Flight Simulation and Control of a Helicopter Undergoing Rotor Span Morphing

Jayanth Krishnamurthi [*] **Farhan Gandhi** [†]

Rotorcraft, Adaptive, and Morphing Structures (RAMS) Lab
Rensselaer Polytechnic Institute
Troy, NY 12180, USA

Abstract

This study focuses on the flight simulation and control of a helicopter undergoing rotor span morphing. A model-following dynamic inversion controller with inner and outer loop Control Laws (CLAWS) is implemented, and radius change is introduced as a feedforward component to the inner loop CLAWS. Closed-loop poles associated with the low-frequency aircraft modes are observed to be robust to change in rotor span, eliminating the need for model updates due to span morphing during the dynamic inversion process. The error compensators in the CLAWS use PID control for roll and pitch attitude, PI control for yaw rate and lateral and longitudinal ground speed, but require PII control for vertical speed to avoid altitude loss observed with only PI control, during span morphing. Simulations are based on a span-morphing variant of a UH-60A Black Hawk helicopter at 18,300 lbs gross-weight and 40 kts cruise. From a baseline rotor radius of 26.8 ft, retraction to 22.8 ft, as well as extension to 31.5 ft is considered, nominally over a 60 sec duration. The controller is observed to regulate the longitudinal, lateral and vertical ground speeds well over the duration of the span morphing. Further, the controller is observed to maintain its effectivess in regulating the ground speeds when the span morphing duration is reduced to 30 sec.

1. INTRODUCTION

With the optimum rotor geometry known to vary depending on the operating state, a fixed-geometry rotor can perform optimally in a specific set of conditions with significant penalties in other conditions, or alternatively, represent a compromise design with adequate but suboptimal performance in most conditions. Recently, there has been significant interest in rotor morphing, or reconfiguration, to enhance performance in diverse operating conditions, as well as expand the flight envelope and operational flexibility of rotary-wing aircraft. Although rotor morphing faces substantially greater challenges than morphing in fixed-wing aircraft due to a smaller available area in which to fit the actuators and morphing mechanisms, requirement for these to operate in the presence of a large centrifugal field, and requirement for power transfer to the rotating system, the potential payoff is even greater.

Among the various "types" of rotor morphing considered in the literature, rotor span morphing is perhaps the most intriguing, with both maximum risk as well as reward. Rotor span morphing was first considered as far back as in the 1960's[1,2], and received a second close look-in in the 1990's for application to tiltrotor aircraft[3,4]. While the benefit of rotor span variation is immediately evident on a tiltrotor aircraft (with a larger span preferred for operation in helicopter mode, and reduced span for operation in propeller mode), span variation can also be highly advantageous for conventional edgewise rotors. It is well understood that the hover performance of a conventional helicopter improves significantly with increase in rotor diameter[5,6,7] but the larger footprint may be limiting in space-constrained environ-

[*] Graduate Research Assistant
[†] Redfern Professor in Aerospace Engineering
Presented at the 41st European Rotorcraft Forum, Munich, Germany, Sept. 1-4, 2015

ments (e.g., shipboard operation). Span variation allows operation in tight spaces, albeit at a reduced efficiency, as well as at a significantly increased efficiency when the aircraft moves to an unconstrained environment. Span morphing can also offer significant benefit in very high-speed cruise. Slowed-rotor compound helicopters transfer the lifting function from the rotor to the fixed-wing in high-speed cruise and reducing rotor diameter reduces the overall rotor drag as well susceptibility to aeroelastic instability and gusts. The Boeing Company, funded by DARPA, recently developed the DiscRotor technology where nested rotor blades were retracted for high-speed operation. Other efforts have focused on design and demonstration of span-morphing rotors[5,8,9,10].

The studies described on rotor morphing have thus far focused broadly on quantifying performance benefits and demonstrating implementation methods. However, transient behavior and control of the aircraft during the morphing process has received little attention so far. A helicopter undergoing rotor morphing will naturally tend to leave its trimmed flight condition. In order for the aircraft to maintain its current operating condition (speed, altitude, heading, etc.), the primary controls would need to be simultaneously exercised as the rotor morphs. The current study addresses this gap in knowledge and focuses on the design and application of a model-following dynamic inversion controller to maintain the aircraft's current operating state during rotor span morphing. Simulation results are provided for a UH-60A Black Hawk helicopter at 40 knots cruise to demonstrate the effectiveness of the controller during morphing, and differences between the baseline and the morphed states are discussed as well.

2. SIMULATION MODEL

A simulation model for the UH-60A Black Hawk has been developed in-house, with components based on Sikorsky's GenHel model[11].The model is a non-linear, blade element representation of a single main rotor with articulated blades with airfoil table look-up. The blades themselves are individually formulated as rigid bodies undergoing rotations about an offset flapping hinge. The lag degree of freedom is neglected. The 3-state Pitt-Peters dynamic inflow model[12] is used to represent the induced velocity distribution on the rotor disk. The tail rotor forces and torque are based on the closed-form Bailey rotor model[13]. The rigid fuselage and empennage (horizontal and vertical tail) forces and moments are implemented as look-up tables based on wind tunnel data from the GenHel model[11]. A simple 3-state generic turbine engine model given by Padfield[14] is used for the propulsion dynamics, with the governing time constants approximated based on the GenHel engine model[11].

The nonlinear dynamics for the baseline aircraft are written as

$$\dot{\vec{x}} = f(\vec{x}, \vec{u}) \qquad (1)$$
$$\vec{y} = g(\vec{x}, \vec{u})$$

where $\vec{y}$ is a generic output vector. The state vector, $\vec{x}$, is given by

$$\vec{x} = [u, v, w, p, q, r, \phi, \theta, \psi, X, Y, Z, \qquad (2)$$
$$\beta_0, \beta_{1s}, \beta_{1c}, \beta_d, \dot{\beta}_0, \dot{\beta}_{1s}, \dot{\beta}_{1c}, \dot{\beta}_d, \lambda_0, \lambda_{1s}, \lambda_{1c},$$
$$\Omega, \chi_f, Q_e]^T$$

The state vector comprises of 12 fuselage states (3 body velocities (u, v, w), 3 rotational rates (p, q, r), 3 attitudes (ϕ, θ, ψ), and 3 inertial positions (X, Y, Z), 11 rotor states (4 blade flapping states $(\beta_0, \beta_{1s}, \beta_{1c}, \beta_d)$ and their derivatives in multi-blade coordinates, and 3 rotor inflow states $(\lambda_0, \lambda_{1s}, \lambda_{1c})$) and 3 propulsion states (rotational speed (Ω), engine fuel flow (χ_f) and engine torque (Q_e). The control input vector is given by

$$\vec{u} = [\delta_{lat}, \delta_{long}, \delta_{coll}, \delta_{ped}, \delta_{tht}]^T \qquad (3)$$

and is comprised of lateral, longitudinal, and collective stick inputs to the main rotor, pedal input to the tail rotor, and throttle input to the engine.

2.1. Baseline Model Validation

The baseline simulation model was validated against a trim sweep of flight test and GenHel data[15]. For validation purposes alone, elastic twist deformations on the blades, based on an empirical correction from the GenHel model[11], were incorporated to improve the correlation of the simulation model. Figure 1 shows representative results and the baseline simulation model correlates well with both flight test and GenHel.

For the design of control laws, the nonlinear equations of motion were linearized using numerical perturbation at specific operating conditions. The linearized version of Equation 1 can be written as

$$\Delta\dot{\vec{x}} = A\Delta\vec{x} + B\Delta\vec{u} \qquad (4)$$
$$\Delta\vec{y} = C\Delta\vec{x} + D\Delta\vec{u}$$

The linearized model was subsequently validated against GenHel[15] and flight data[16] and Figure 2 shows

representative results for hover and 80 knots forward flight. The model correlates fairly well in the frequency range of 0.4-10 rad/sec for both cases, as shown.

2.2. Variable Span Rotor Blade

The baseline UH-60A simulation blade is now modified to create a span morphing variant, based on prior work done by Mistry and Gandhi[7]. The geometry is described in Ref.7 in detail but a brief overview is presented here. Figure 3 shows the blade twist, chord, and mass distribution for the baseline and variable span blades. In Figure 3(a), a significant portion of the baseline blade has a constant twist rate. An implementation of variable span would work best for a constant twist rate and the span morphing was thus limited to the linearly twisted section of the blade. This is reflected in Figure 3(b) and shows the twist distribution of the variable span blade in its retracted, nominal, and extended configurations. In Figure 3(b), while the twist rate is identical between the inboard fixed and sliding sections, the nose-down twist at the tip of the blade relative to the root will vary with radius. Figure 3(c) shows the chord distribution of the variable span blade. As seen in the figure, the sliding section has a lower chord in order to enable full retraction with some reasonable tolerance. Figure 3(d) shows the mass distribution of the variable span blade. The total mass is increased by approximately 36% relative to the baseline blade to account for the actuation mechanism/assembly.

With this modified blade, we now introduce a span morphing input into the dynamics given by Equation 1. The equations of motion now become

$$\dot{\vec{x}} = f\left(\vec{x}, \vec{u}_1, \vec{u}_2\right) \qquad \vec{y} = g\left(\vec{x}, \vec{u}_1, \vec{u}_2\right) \tag{5}$$

where u_1 is now the primary input vector given by Equation 3 and u_2 is the morphing input vector given by

$$\vec{u}_2 = R_{span} \tag{6}$$

Correspondingly, the linear model for the baseline aircraft given by Equation 4 now becomes

$$\Delta\dot{\vec{x}} = A\Delta\vec{x} + B_1\Delta\vec{u}_1 + B_2\Delta\vec{u}_2 \qquad \Delta\vec{y} = C\Delta\vec{x} + D_1\Delta\vec{u}_1 + D_2\Delta\vec{u}_2 \tag{7}$$

where B_1 and B_2 are the control matrices that correspond to the primary and morphing input vectors, respectively.

3. CONTROL SYSTEM DESIGN

The design of the control system is based on model following linear dynamic inversion (DI)[17]. Model following concepts are widely used in modern rotorcraft control systems for their ability to achieve task-tailored handling qualities via independently setting feed-forward and feedback characteristics[18]. In addition, the dynamic inversion controller does not require gain scheduling since it takes into account the nonlinearities and cross-couplings of the aircraft (i.e. a model of the aircraft is built into the controller). It is thus suitable for a wide range of flight conditions[17].

A schematic of the overall control system is shown in Figure 4. The control system is effectively split into inner and outer loop control laws (CLAWS). In designing the CLAWS, the full 26-state linear model given by Equation 7 was reduced to an 8-state quasi-steady model. Firstly, the rotor RPM degree of freedom (Ω) is assumed to be regulated via the throttle input determined by the RPM Governor (subsection 3.3), with the remaining propulsion states (χ_f and Q_e) coupling only with Ω. Therefore, the propulsion states and throttle input are truncated from the linear model. Secondly, since the rotor dynamics are considerably faster than the fuselage dynamics, they can essentially be considered as quasi-steady states and folded into the fuselage dynamics[14], which reduces computational cost. The resulting system is an effective 8-state quasi-steady model whose state and control vectors are given by

$$\Delta\vec{x}_r = [\Delta u, \Delta v, \Delta w, \Delta p\, \Delta q, \Delta r, \Delta\phi, \Delta\theta]^T \qquad \Delta\vec{u}_{1r} = [\Delta\left(\delta_{lat}\right), \Delta\left(\delta_{long}\right), \Delta\left(\delta_{coll}\right), \Delta\left(\delta_{ped}\right)]^T \qquad \Delta\vec{u}_2 = [\Delta R_{span}]^T \tag{8}$$

In this reduced-order model, the output vector is set up such that it contains only the states themselves or contains quantities which are a function of only the states. Therefore, the matrices D_1 and D_2 given in Equation 7 are eliminated from the model structure. In addition, note that while the controller uses a reduced-order linear model, its performance was ultimately tested with the full nonlinear model given by Equation 5.

3.1. Inner Loop CLAW

A diagram of the inner loop CLAW is shown in Figure 5. In the inner loop, the response type to pilot input is designed for Attitude Command Attitude Hold (ACAH) in the roll and pitch axis, where pilot input commands a change in roll and pitch attitudes ($\Delta\phi_{cmd}$ and

$\Delta\theta_{cmd}$) and returns to the trim values when input is zero. The heave axis response type is designed for Vertical Speed Command Height Hold (VCHH), where pilot input commands a change in rate-of-climb and holds current height when the rate-of-climb is zero. The yaw axis response type is designed for Rate Command Heading Hold (RCHH), where pilot input commands a change in yaw rate and holds current heading when yaw rate is zero. These are based on ADS-33E specifications for hover and low-speed forward flight ($V \leq 45$ knots)[19].

The commanded values (shown in Figure 5) are given by

$$\Delta\vec{y}_{inner,cmd} = \begin{bmatrix} \Delta\phi_{cmd} \\ \Delta\theta_{cmd} \\ \Delta V_{Z_{cmd}} \\ \Delta r_{cmd} \end{bmatrix} \tag{9}$$

They are subsequently passed through command filters, which generate the reference trajectories ($\Delta\vec{y}_{ref}$) and their derivatives ($\Delta\dot{\vec{y}}_{ref}$) (see Figure 5). The parameters of the command filter were selected to meet Level 1 handling qualities specifications (bandwidth and phase delay) given by ADS-33E for small amplitude response in hover and low-speed forward flight[19]. Table 1 shows the parameters used in the command filters in the inner loop CLAW, where the roll and pitch axes use second-order filters and the heave and yaw axes use first-order filters.

Table 1: Inner Loop Command Filter Parameters

Command Filter	ω_n (rad/sec)	ζ	τ (sec)
Roll	2.5	0.8	-
Pitch	2.5	0.8	-
Heave	-	-	2
Yaw	-	-	0.4

In dynamic inversion, the technique of input-output feedback linearization is used, where the output equation ($\Delta\vec{y}_{inner}$ in Equation 10) is differentiated until the input appears explicitly in the derivative[17,20]. The inversion model implemented in the controller uses the 8-state vector given by Equation 8. Writing the reduced-order linear model in state space form, we have

$$\begin{aligned} \Delta\dot{\vec{x}}_r &= A_r\Delta\vec{x}_r + B_{1r}\Delta\vec{u}_{1r} + B_{2r}\Delta\vec{u}_2 \\ \Delta\vec{y}_{inner} &= C_r\Delta\vec{x}_r \end{aligned} \tag{10}$$

where the A_r matrix is 8x8, B_{1r} is 8x4, B_{2r} is 8x1, C_r matrix is 4x8, and the output vector $\Delta\vec{y}_{inner}$ is 4x1.

Applying dynamic inversion on Equation 10 results in the following control law

$$\Delta\vec{u}_{1r} = \left[C_r A_r^{k-1} B_{1r}\right]^{-1} \left(\nu - \left[C_r A_r^{k}\right]\Delta\vec{x}_r - \left[C_r A_r^{k-1} B_{2r}\right]\Delta\vec{u}_2\right) \tag{11}$$

where k = 2 for the roll and pitch axes, and k = 1 for the heave and yaw axes. The term $\left[C_r A_r^{k-1} B_{2r}\right]\Delta\vec{u}_2$ is an additional feedforward component due to the morphing input. The term ν is known as the "pseudo-command" vector or an auxiliary input vector, shown in Figure 5. The psuedo-command vector is a sum of feedforward and feedback components. It is defined as

$$\nu = \begin{bmatrix} \nu_\phi \\ \nu_\theta \\ \nu_{V_Z} \\ \nu_r \end{bmatrix} = \Delta\dot{\vec{y}}_{ref} + [K_P\ K_D\ K_I] \begin{bmatrix} e \\ \dot{e} \\ \int e\,dt \end{bmatrix} \tag{12}$$

where the error vector, denoted as e (see Figure 5) is given by

$$e = \Delta\vec{y}_{ref} - \Delta\vec{y}_{inner} \tag{13}$$

The variables K_P,K_D, and K_I indicate the proportional, derivative, and integral gains in a PID compensator.

Note that the application of dynamic inversion in Equation 10 is carried out in the body reference frame. In Equation 12, the pseudo-commands ν_ϕ, ν_θ, and ν_r are prescribed in the body frame, while ν_{V_Z} is in the inertial frame. Therefore, a transformation was introduced to change the heave axis pseudo-command to the body frame[21] prior to inversion, and is given by

$$\nu_w = \frac{\nu_{V_Z} + u\dot{\theta}\cos\theta}{\cos\theta\cos\phi} \tag{14}$$

If the reduced-order model given by Equation 10 were a perfect representation of the flight dynamics, the resulting system after inversion would behave like a set of integrators and the pseudo-command vector would not require any feedback compensation. In practice, however, errors between reference and measured values arise due to higher-order vehicle dynamics and/or external disturbances and therefore require feedback to ensure stability.

The PID compensator gains are selected to ensure that the tracking error dynamics due to disturbances or modeling error are well regulated. A typical choice for the gains is that the error dynamics be on the same order as that of the command filter model for each axis. Table 2 shows the compensator gain values used in each axis.

Table 2: Inner Loop Error Compensator Gains

	K_P	K_D	K_I
Roll	10 (1/sec^2)	5.75 (1/sec)	4.6875 (1/sec^2)
Pitch	10 (1/sec^2)	5.75 (1/sec)	4.6875 (1/sec^2)
Heave	1 (1/sec)	0	0.25 (1/sec^2)
Yaw	1 (1/sec)	0	6.25 (1/sec^2)

Finally, the vector $\Delta\vec{u}_{1r}$ from Equation 11 is added to the trim values of $\vec{u}_{1r}$ before being passed into the control mixing unit of the aircraft.

3.2. Outer Loop CLAW

In order to maintain trimmed forward flight, an outer loop is designed to regulate lateral (V_Y) and longitudinal (V_X) ground speed while the aircraft is morphing. A schematic of the outer loop CLAW is shown in Figure 6. Note that the overall structure is similar to the inner loop. The response type for the outer loop is translational rate command, position hold (TRC/PH), where pilot input commands a change in ground speed and holds current inertial position when ground speeds are zero. With the implementation of the outer loop, the pilot input does not directly command $\Delta\phi_{cmd}$ and $\Delta\theta_{cmd}$ as in the inner loop CLAW. Rather, they are indirectly commanded through the desired ground speeds (see Figure 4).

The commanded values in the outer loop (shown in Figure 6) are given by

$$\Delta\vec{y}_{outer,cmd} = \begin{bmatrix}\Delta V_{X_{cmd}} \\ \Delta V_{Y_{cmd}}\end{bmatrix} \tag{15}$$

and passed through first-order command filters. Similar to the inner loop, the parameters of the command filter are selected based on ADS-33E specifications in hover and low-speed forward flight[19].

Table 3: Outer Loop Command Filter Parameters

Command Filter	τ (sec)
Lateral (V_Y)	2.5
Longitudinal (V_X)	2.5

In the outer loop, to achieve the desired ground speeds, the required pitch and roll attitude command input to the inner loop (Equation 9) is determined through model inversion[17,22]. A simplified linear model of the lateral and longitudinal dynamics is extracted from Equation 10 and is given by

$$\Delta\dot{\vec{x}}_{r,outer} = A_{TRC}\Delta\vec{x}_{r,outer} + B_{TRC}\begin{bmatrix}\Delta\phi_{cmd} \\ \Delta\theta_{cmd}\end{bmatrix} \tag{16}$$
$$\Delta\vec{y}_{outer} = \begin{bmatrix}\Delta V_X \\ \Delta V_Y\end{bmatrix} = C_{TRC}\Delta\vec{x}_{r,outer}$$

with A_{TRC}, B_{TRC}, and $\Delta\vec{x}_{r,outer}$ defined as

$$A_{TRC} = \begin{bmatrix}X_u & X_v \\ Y_u & Y_v\end{bmatrix} \tag{17}$$
$$B_{TRC} = \begin{bmatrix}0 & -g \\ g & 0\end{bmatrix}$$
$$\Delta\vec{x}_{r,outer} = \begin{bmatrix}\Delta u \\ \Delta v\end{bmatrix}$$

where u and v are body-axis velocities, X_u, X_v, Y_u, and Y_v are stability derivatives and g is the gravitational acceleration. Applying dynamic inversion on this model results in the following control law

$$\begin{bmatrix}\Delta\phi_{cmd} \\ \Delta\theta_{cmd}\end{bmatrix} = \tag{18}$$
$$(C_{TRC}B_{TRC})^{-1}\left(\nu - C_{TRC}A_{TRC}\Delta\vec{x}_{r,outer}\right)$$

The pseudo-command vector, $\nu = \begin{bmatrix}\nu_{V_X} \\ \nu_{V_Y}\end{bmatrix}$, is defined similarly to Equation 12, with the error dynamics also defined in a manner similar to that of the inner loop. The PID compensator gains for the outer loop are given in Table 4.

Table 4: Outer Loop Error Compensator Gains

	K_P (1/sec)	K_D	K_I (1/sec^2)
Lateral (V_Y)	0.8	0	0.16
Longitudinal (V_X)	0.8	0	0.16

3.3. RPM Governor

A rotor that is undergoing span morphing will definitely impact the rotational degree of freedom (Ω). On the UH-60A and in the GenHel model, the rotor RPM is regulated by a complex, nonlinear engine Electrical Control Unit (ECU)[11]. Since a simplified modeling of the propulsion dynamics is used in this study, a simple PI controller, with collective input feedforward from the inner loop CLAW, is implemented to regulate the rotor RPM via the throttle input, which is mapped to the fuel flow state (χ_f). The controller is similar in structure to the one given by Kim[23]. A schematic of the RPM Governor is shown in Figure 7. In Figure 7, the gains K_P and K_I

were approximated based on the GenHel model's ECU. The collective feedforward gain, K_C, was approximated using a mapping between throttle and collective input, based on trim sweep results of the baseline aircraft in subsection 2.1. Table 5 shows the gains used in the governor.

Table 5: RPM Governor Gains

	K_P (%/(rad/sec))	K_I (%/rad)	K_C (nd)
Ω	3	5	1.2

4. RESULTS & DISCUSSION

4.1. Heave Axis Error Compensator - PI vs PII

The aircraft was trimmed in hover with a gross weight of 18,300 lbs. and the blades were retracted from a nominal radius of $R_{span} = 26.8$ ft to $R_{span} = 22.8$ ft over 60 seconds. It was observed that the controller was not able to compensate adequately in the heave axis. This is because of the parabolic nature[24] of the disturbance in vertical velocity due to span morphing. The vertical speed and inertial position of the aircraft with the PI controller is shown in Figure 8, indicated by the black dashed lines. Though the overall deviation in vertical speed is small in Figure 8(a) for the PI compensator, the aircraft slowly descends approximately 27 feet over the duration of the morphing (see Figure 8(b)). As a solution, the PI compensator was replaced with a proportional-double integral compensator (PII), which is of the form

$$K(s) = K_P + \frac{K_I}{s} + \frac{K_{II}}{s^2} \tag{19}$$

The gains were selected empirically, with K_P and K_I being close to the original PI compensator values. Table 6 shows the gains used in the compensator. Comparing the two compensators in Figure 8, it can be seen that the drift in altitude is considerably reduced. The small drift with the PII (less than 8 ft) is attributed to an imperfect inversion. In the forthcoming sections of results for 40 knots retraction and extension, the simulations were run with the PII compensator in the heave axis.

Table 6: Heave Axis PII Compensator Gains

	K_P (1/sec)	K_I (1/sec^2)	K_{II} (1/sec^2)
V_Z	1.1	0.35	0.025

4.2. Effect of Span Morphing on Dynamic Modes and Robustness of Controller

The introduction of span morphing is expected to affect the dynamic modes of the aircraft. Figure 9 shows the bare airframe (open-loop) eigenvalues of the full-order model (Equation 7) at 40 knots, for both retraction and extension. The change in rotor radius noticeably alters the rotor flap and inflow modes, as would be expected. However, note that there is relatively very little movement of the fuselage modes. Since the characteristic frequencies of the fuselage and rotor dynamics are separated by 1-2 orders of magnitude, there is relatively light coupling between the rotor and fuselage modes. Consequently, little movement of the fuselage modes is observed.

The dynamic inversion controller uses a reduced-order version of the bare airframe model (see Equation 8) containing quasi-steady fuselage dynamics. As mentioned in subsection 3.1, the application of model inversion in the inner loop CLAW effectively changes the plant dynamics into a decoupled set of integrators, which are then stabilized with feedback control. Using a quasi-steady model at the nominal radius ($R = 26.8$ ft), the closed-loop dynamics of the system with this controller are shown in Figure 10 for 40 knots, where for clarity, only the eigenvalues close to the imaginary axis are shown. In both cases (retraction and extension), the controller is robust to changes in span, particularly for the critical eigenvalues that are very close to the imaginary axis. Based on these observations, the controller was run with a single quasi-steady model at the nominal radius and found to be sufficient for both retraction and extension, without requiring any model updates during the inversion process.

4.3. 40 knots - Retraction

This section presents simulation results for a UH-60A Black Hawk helicopter at 18,300 lbs gross weight undergoing rotor span retraction while cruising at 40 kts airspeed. The span is reduced from R_{span} of 26.8 ft to 22.8 ft over a 60 second interval (see Figure 11(a)). Figures 11(b) and 11(c) show the variation in main rotor thrust and torque associated with the span retraction. It is observed that the thrust is regulated well during the duration of the morphing. The increase in rotor torque bears greater scrutiny and is discussed in detail toward the end of this section.

Figure 12 presents the variation in main rotor collective, longitudinal and lateral cyclic pitch, tail rotor collective, and aircraft roll and pitch attitudes, over the duration of the rotor span retraction. Also presented in

Table 8 are the control and fuselage attitude values corresponding to the baseline span and retracted configurations. Figure 13 presents the variation in rotor coning and longitudinal and lateral cyclic flapping during rotor span retraction. An increase in root collective pitch from 15.6 deg to 18.3 deg (Figure 12(a)) is required for the contracted rotor to be able to generate the necessary lift. Since the centrifugal force on the blades decreases as the span is reduced, the coning angle is seen to increase, as expected (Figure 13(a)).

The increase in tail rotor collective (Figure 12(d)) with span retraction is consistent with the increase in main rotor torque seen in Figure 11(c). The larger lateral force due to increase in tail rotor thrust, as well as the increased roll moment it generates due to its location above the aircraft CG affects the lateral force and roll moment equilibrium of the aircraft. Both the rotor lateral flapping (Figure 13(c)) and lateral cyclic pitch (Figure 12(c)) are seen to increase in magnitude, and a slight change in aircraft roll attitude (Figure 12(e)) is observed, as well. Due to the tail rotor cant angle on the UH-60A Black Hawk helicopter[11], the increase in tail rotor thrust also produces a nose-down pitching moment on the aircraft. The rotor longitudinal cyclic flapping (forward tilt of the tip path plane) is also seen to increase (Figure 13(b)), and a corresponding increase in longitudinal cyclic pitch is observed (Figure 12(b)). However, the forward tilting of the tip path plane along with an increased overall downwash for the retracted rotor changes the main rotor wake skew angle resulting in a reduced upload on the horizontal stabilator. This results in a net increase in nose-up pitch attitude of the aircraft, as seen in Figure 12(f).

Figure 14 shows time histories of the aircraft velocities and altitude over the duration of the rotor retraction. Note that the lateral and longitudinal ground speeds are controlled by the outer loop CLAW (subsection 3.2) while the vertical speed is controlled by the inner loop CLAW (subsection 3.1). As seen in the figure, they are well regulated by the controller. The maximum loss in altitude during the morphing process, with the use of PII control in the heave axis, is observed to be about 8 ft. Figure 15 shows the time history of rotor RPM during blade retraction. Although only a very small drift in RPM is observed over the duration of the morphing, the drift is not fully rejected as rotor span morphing manifests as a higher-order disturbance to the PI compensator (Figure 7).

Figure 16 shows disk plots of the inflow angle and blade sectional angle of attack over the rotor disk, for both the baseline rotor as well as the rotor in the retracted configuration. An increase in angle of attack seen over the entire rotor disk when the rotor is retracted (compare Figures 16(c) and 16(d)) allows generation of the necessary lift for aircraft trim. From a momentum theory standpoint, an increased disk loading corresponding to a smaller rotor area is expected to produce a larger overall downwash. Increased lateral and longitudinal flapping for the retracted rotor (Figures 13(c) and 13(b)) further increases downwash velocities over portions of the rotor disk. The combination of these factors results in an increase in downwash velocities and consequently inflow most prominently in the fourth quadrant of the rotor disk when the span is retracted (compare Figures 16(a) and 16(b)).

Figure 17 shows disk plots of the induced and profile drag over the rotor disk, for both the baseline rotor as well as the rotor in the retracted configuration. Comparing Figures 17(a) and 17(b), the induced drag for the retracted rotor is seen to be significantly higher, predominantly over the fourth quadrant of the rotor disk, but spilling over into the first and third quadrants, as well. The areas of largest increase in induced drag are generally consistent with the areas displaying the largest increases in inflow angle (Figures 16(a) and 16(b)). Table 7 presents the induced, profile and total rotor power for the baseline (26.8 ft radius) case, as well as the retracted (22.8 ft radius) configuration. The induced power requirements for the retracted rotor is seen to increase to 1140 HP (compared to 853.9 HP for the baseline). The profile power, on the other hand, reduces to 252 HP (from 340.7 HP for the baseline). In Figure 17(d) although the profile drag over the outboard regions of the retracted rotor are higher than the baseline rotor experiences over the same radial range (attributed to higher angles of attack), the absence of the outer rim operating at the highest Mach numbers reduces the overall profile drag. The increase in total power from 1194.6 HP for the baseline to 1392.9 HP for the retracted rotor is consistent with the increase in main rotor torque presented in Figure 11(c) (with the rotor RPM remaining unchanged).

4.4. 40 knots - Extension

Next, simulations were conducted for the UH-60A Black Hawk helicopter undergoing rotor span extension (with the aircraft gross weight at 18,300 lbs and cruise speed at 40 kts, as in the previous section). The span is extended from the baseline 26.8 ft to 31.5 ft over a 60 second interval (see Figure 18(a)). Figures 18(b) and 18(c) show the variation in main rotor thrust and torque associated with the span retraction. As in the case of span retraction (Figure 11(b)) the thrust is regulated well over the duration of the span extension. An increase in rotor

torque is observed in Figure 18(c) and is examined in further detail below.

Figure 16 shows comparisons of the blade sectional angle of attack over the rotor disk, for the baseline and the fully extended rotor. From Table 8, it is observed that the reduction in rotor collective pitch accompanying span extension is significantly smaller than the increase in collective pitch that accompanied span retraction. Further, Figure 19(b) shows that the outboard sections of the extended rotor are operating at negative angles of attack, due to the increased negative twist in the vicinity of the blade tip compared to the baseline blade (see Figure 3(b)). Because of the loss in lift in the outer regions of the rotor disk, the angles of attack in the inboard sections are actually slightly higher than the baseline (compare Figures 19(a) and 19(b)). Figure 20 shows a comparison of the elemental induced and profile drag distributions over the rotor disk for baseline rotor and the extended configuration. For the extended rotor, the lower disk loading generally results in lower values of induced drag over the rotor disk (compare Figures 20(a) and 20(b)). With span extension, the profile drag at the tips is the highest due to the higher tip Mach numbers than the baseline, but the profile drag is also observed to be higher in the inboard sections due to the higher angles of attack (Figures 20(c) and 20(d)). Table 7 shows a very large increase in profile power for the extended rotor (931.5 HP compared to 340.7 HP for the baseline), due to the increase in profile drag observed in Figure 20. Although the induced power reduces for the extended rotor, the increase in profile power dominates, resulting in an overall increase in total power to 1572.2 HP (compared to 1392.9 HP for the baseline). The increase in power requirement for the extended rotor (with its higher advancing tip Mach number driving profile power increases) is greater than that observed for the retracted rotor (with its higher disk loading driving induced power increases). Correspondingly, the increase in rotor torque with span extension (in Figure 18(c)) is observed to be greater than the increase in rotor torque with span retraction (in Figure 11(c)).

Figure 21 presents the variation in main rotor collective, longitudinal and lateral cyclic pitch, tail rotor collective, and aircraft roll and pitch attitude, over the duration of the rotor span extension. The control and fuselage attitude values in the fully extended configuration are also included in Table 8. The change in rotor root collective pitch in Figure 21(a) is particularly interesting, first decreasing slightly from its baseline value of 15.6 deg to about 15.24 deg as the rotor expands, then reversing course and increasing to a value of 15.38 deg at full extension. The reduction in collective is anticipated as the span begins increasing, but as the angles of attack at the blade tips become negative and the tips generate negative lift, the collective pitch increases to counteract this effect. The changes in longitudinal and lateral cyclic pitch, and aircraft pitch and roll attitude, are of opposite sense to those seen in the case of span retraction (compare Figures 21(b),21(c),21(e) and 21(f) to the corresponding plots in Figure 12). The increase in tail rotor collective with span extension (Figure 21(d)) is consistent with the torque increase discussed in the preceding paragraph. Figure 22 presents the variation in rotor coning and longitudinal and lateral cyclic flapping during rotor span extension. The increase in centrifugal force on the extended rotor reduces the rotor coning (Figure 22(a)), and the changes in longitudinal and lateral cyclic flapping are of opposite send those seen in the case of span retraction (compare Figures 13 and 22).

Figure 23 shows time histories of the aircraft velocities and altitude over the duration of the rotor extension. As in the case of span retraction, the velocities are well regulated by the controller. While a loss in altitude is intuitively expected with rotor span retraction, altitude might be expected to increase with rotor span extension. However, Figure 23(d) shows a maximum 5 ft loss in altitude during the span extension process with the use of PII control in the heave axis. It is hypothesized that this is due to the controller over-compensating for the increase in lift due to span extension. Figure 24 shows the time history of rotor RPM during blade extension. As in the case of span retraction in the previous section (Figure 15) only a very small drift in RPM is observed over the duration of the morphing.

4.5. Rate of Morphing

The results in the previous section considered rotor span retraction and extension over a 60 second time interval. This section examines the impact of reduction in morphing duration to 30 seconds as well as an increase to 90 seconds. Furthermore, the preceding results used a PII controller for vertical velocity in the inner loop CLAW. With PI controllers used for longitudinal and lateral ground speeds and yaw rate, the effect of using the original PI controller for vertical velocity (Table 2), as well, is examined in this section.

Figure 25 shows the three rotor span retraction profiles considered, over 30, 60 and 90 second durations. Figures 25(b)-25(d) show time histories of the aircraft altitude corresponding to cases of span retraction over 30, 60 and 90 second intervals, respectively. While PI control on the heave axis eliminates steady-state error on vertical velocity, a steady state error on altitude is observed. Regardless of the duration of morphing, a

total altitude loss of over 27 ft is observed with the PI controller. A PII controller on vertical velocity is equivalent to a PID type control on altitude, thereby eliminating steady-state error in altitude. Although a small initial loss in altitude is observed, Figures 25(b)-25(d) show that this is quickly recovered. The maximum transient loss in altitude decreases with increase in morphing duration (from 11 ft for a 30 second morph, to 8 ft for a 60 second morph, and 6 ft for a 90 second morph).

Figure 26 presents similar results for the case of rotor span extension. With the PI controller, a steady-state 20 ft loss in altitude is observed, for all three morphing durations considered. With the PII controller, steady state error in altitude is eliminated, and as with the case of span retraction, the transient loss in altitude reduces with increase in duration over which span extension is introduced (from 9 ft for 30 a 30 second morph, to 5 ft for a 60 second morph, and 3.5 ft for a 90 second morph). It was verified that the other aircraft responses such as rotor thrust, torque, RPM and lateral and longitudinal ground speeds continue to be well regulated (results not included in the paper) even when the morphing duration was reduced.

5. CONCLUSIONS

This study focuses on the flight simulation and control of a helicopter undergoing rotor span morphing. A model-following dynamic inversion controller with inner and outer loop Control Laws (CLAWS) is implemented, and radius change is introduced as a feedforward component to the inner loop CLAWS. Simulation results are presented based on a span-morphing variant of a UH-60A Black Hawk helicopter at 18,300 lbs gross-weight and 40 kts cruise. From a baseline rotor radius of 26.8 ft, retraction to 22.8 ft, as well as extension to 31.5 ft is considered, nominally over a 60 sec duration. From the results presented in the paper the following observations were drawn:

1. Closed loop poles associated with the low-frequency aircraft modes were robust to change in rotor span, eliminating the need for model updates due to span morphing during the dynamic inversion process.

2. The error compensators in the CLAWS use PID control for roll and pitch attitude, PI control for yaw rate and lateral and longitudinal ground speed. However, using only PI control for vertical speed resulted in altitude loss of up to 27 ft over the duration of rotor span morphing. Instead, using PII control for vertical speed reduced the altitude loss to 8 ft (for a 60 sec morphing duration).

3. The controller regulates the longitudinal, lateral and vertical ground speeds well over the nominal 60 sec duration of the span morphing, and maintains its effectiveness in regulating the ground speeds even when the span morphing duration is reduced to 30 sec. However, the PII controller does even better at limiting loss in altitude when the duration of span morphing is increased.

4. For both span retraction as well as extension, the main rotor torque requirements were seen to increase. In the case of span retraction this was attributed to the large increase in induced power (although the profile power decreased slightly). In the case of span extension, there was a large increase in profile power (due to higher tip Mach numbers) although the induced power reduced somewhat.

5. The rotor collective pitch increased, as expected, in the case of span retraction. In the case of span extension the rotor collective pitch first decreases but then reverses course as the increasing washout results in negative lift in the outboard sections of the rotor.

6. Span extension reduced rotor coning due to higher centrifugal force while the reverse was observed for span retraction. Similarly, changes in aircraft pitch and roll attitude, longitudinal and lateral cyclic pitch and rotor flapping were of opposite sense for rotor span retraction and expansion.

ACKNOWLEDGEMENTS

The authors would like to thank Dr. Joseph Horn from the Pennsylvania State University for his helpful insights and suggestions in the development of the simulation model and design of the controller.

References

[1] Linden, A., Bausch, W., Beck, D., D'Onofrio, M., Flemming, R., Hibyan, E., Johnston, R., Murrill, R.J., and Unsworth, D., ``Variable Diameter Rotor Study,'' Air Force Flight Dynamics Laboratory, Air Force Systems

Command, Wright-Patterson Air Force Base, OH, Report No. AFFDL-TR-71-170, AFFDL, January 1972.

[2] Fenny, C., ``Mechanism for Varying the Diameter of Rotors Using Compound Differential Rotary Transmissions," American Helicopter Society, 61st Annual Forum Proceedings, Grapevine, TX, June 13, 2005.

[3] Fradenburgh, E.A., and Matsuka, D.G., ``Advancing Tiltrotor State-of-the-Art with Variable Diameter Rotors," American Helicopter Society 48th Forum Proceedings, Washington, D.C., June 3-5, 1992.

[4] Studebaker, K., and Matsuka, D.G., ``Variable Diameter Tiltrotor Wind Tunnel Test Results," American Helicopter Society, 49th Forum Proceedings, St. Louis, MO, May 19-21, 1993.

[5] Prabhakar, T., Gandhi, F., and McLaughlin, D., ``A Centrifugal Force Actuated Variable Span Morphing Helicopter Rotor," 63rd Annual AHS International Forum and Technology Display, Virginia Beach, VA, May 1-3, 2007.

[6] Bowen-Davies, G., and Chopra, I., ``Aeromechanics of a Variable Radius Rotor," American Helicopter Society, 68th Annual Forum Proceedings, Fort Worth, TX, May 1-3, 2012.

[7] Mistry M., and Gandhi, F., ``Helicopter Performance Improvement with Variable Rotor Radius and RPM," *Journal of the American Helicopter Society*, vol. 59, 2014. doi: 10.4050/JAHS.59.042010.

[8] Turmanidze, R.S., Khutsishvili, S.N., and Dadone, L., ``Design and Experimental Investigation of Variable-Geometry Rotor Concepts," Adaptive Structures and Materials Symposium, International Mechanical Engineering Congress and Exposition, New York, November 11-16, 2001.

[9] Turmanidze, R.S., and Dadone, L., ``New Design of a Variable Geometry Prop-Rotor with Cable and Hydraulic-System Actuation," American Helicopter Society 66th Forum Proceedings, Phoenix, AZ, May 11-13, 2010.

[10] Misiorowski, M., Gandhi, F., and Pontecorvo, M., ``A Bi-Stable System for Rotor Span Extension in Rotary-Wing Micro Aerial Vehicles," Proceedings of the 23rd AIAA/ASME/AHS Adaptive Structures Conference, AIAA Science and Technology Forum, Kissimmee, FL, January 5-9, 2015.

[11] Howlett, J.J., ``UH-60A Black Hawk Engineering Simulation Program: Volume I - Mathematical Model," NASA CR-166309, 1981.

[12] Peters, D.A., and HaQuang, N., ``Dynamic Inflow for Practical Applications," *Journal of the American Helicopter Society*, vol. 33, pp. 64--66, October 1988.

[13] Bailey, F.J., ``A Simplified Theoretical Method of Determining the Characteristics of a Lifting Rotor in Forward Flight," NACA Report 716, 1941.

[14] Padfield, G.D., *Helicopter Flight Dynamics: The Theory and Application of Flying Qualities and Simulation Modeling*. Blackwell Publishing, 2nd ed., 2007.

[15] Ballin, M.G., ``Validation of a Real-Time Engineering Simulation of the UH-60A Helicopter," NASA TM-88360, 1987.

[16] Fletcher J.W., ``A Model Structure for Identification of Linear Models of the UH-60 Helicopter in Hover and Forward Flight," NASA TM-110362, NASA, 1995.

[17] Stevens, B.L. and Lewis, F.L., *Aircraft Control and Simulation*. John Wiley & Sons, 2nd ed., 2003.

[18] Tischler, M.B. and Remple, R.K., *Aircraft and Rotorcraft System Identification: Engineering Methods with Flight Test Examples*. AIAA, 2nd ed., 2012.

[19] Anonymous, ``Aeronautical Design Standard Performance Specification, Handling Qualities Requirements for Military Rotorcraft," ADS-33E-PRF, USAAMCOM, 2000.

[20] Slotine, J.E. and Li, W., *Applied Nonlinear Control*. Prentice-Hall Inc., 1991.

[21] Horn, J.F., and Guo, W., ``Flight Control Design for Rotorcraft with Variable Rotor Speed," Proceedings of the American Helicopter Society, 64^{th} Annual Forum, Montreal, Canada, April 29-May 1, 2008.

[22] Ozdemir, G.T., *In-Flight Performance Optimization for Rotorcraft with Redundant Controls*. PhD Thesis, The Pennsylvania State University, December 2013.

[23] Kim, F.D., ``Analysis of Propulsion System Dynamics in the Validation of a High-Order State Space Model of the UH-60," AIAA/AHS Flight Simulation Technologies Conference, Hilton Head, S.C., August 24-26, 1992.

[24] Franklin, G.F., Powell, J.D., and Emami-Naeini, A., *Feedback Control of Dynamic Systems*. Pearson Prentice Hall, 6^{th} ed., 2010.

Table 7: Induced, Profile, and Total Rotor Power

Case	P_i (HP)	P_o (HP)	P_{total} (HP)
Baseline (R_{span} = 26.8 ft)	853.9	340.7	1194.6
Retracted (R_{span} = 22.8 ft)	1140	252.9	1392.9
Extended (R_{span} = 31.5 ft)	640.7	931.5	1572.2

Table 8: Rotor Controls and Fuselage Attitudes

Case	θ_0 (deg)	θ_{1s} (deg)	θ_{1c} (deg)	$\theta_{0_{TR}}$ (deg)	ϕ (deg)	θ (deg)
Baseline (R_{span} = 26.8 ft)	15.6	-3.38	1.74	13.80	-1.12	2.35
Retracted (R_{span} = 22.8 ft)	18.3	-5.81	2.40	15.35	-0.93	3.16
Extended (R_{span} = 31.5 ft)	15.37	-1.64	1.40	15.53	-2.23	1.18

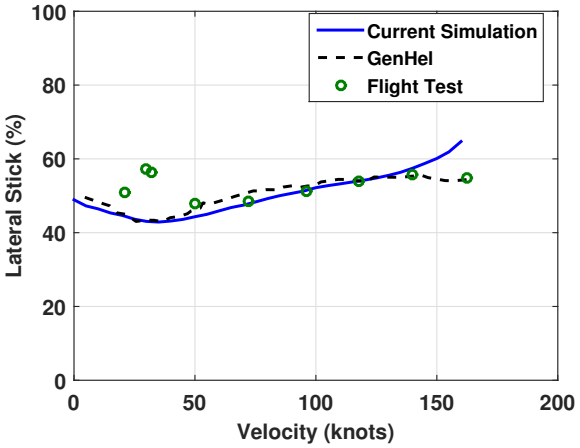

(a) Lateral Stick

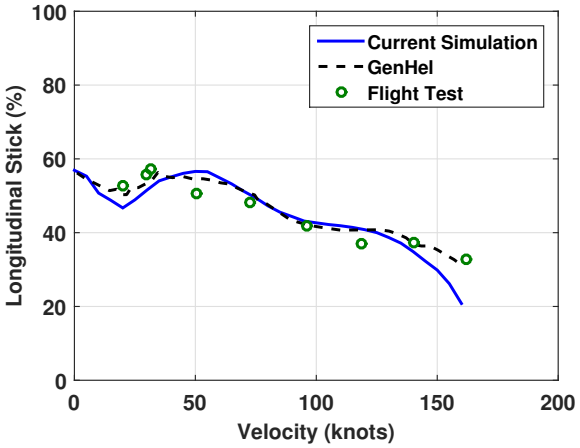

(b) Longitudinal Stick

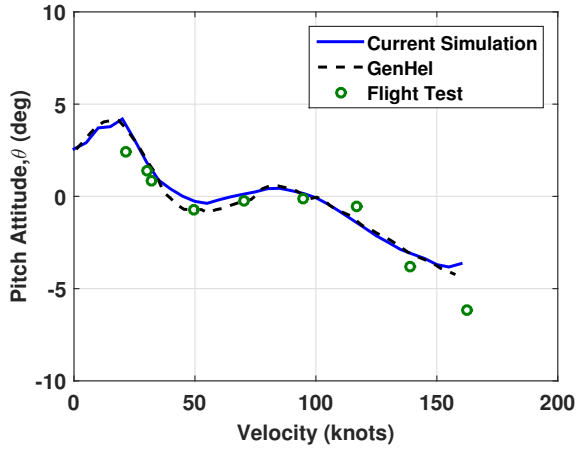

(c) Pitch Attitude

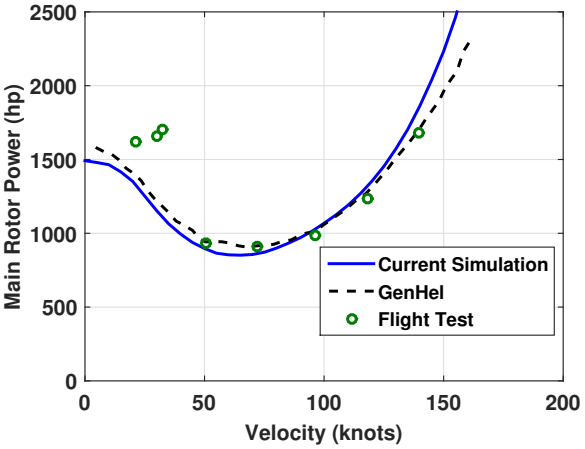

(d) Main Rotor Power

Fig. 1: Baseline UH-60A Trim Sweep Validation

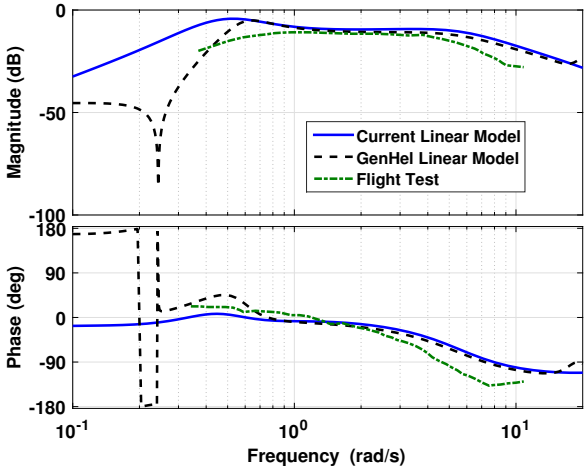

(a) Hover - p/δ_{lat}

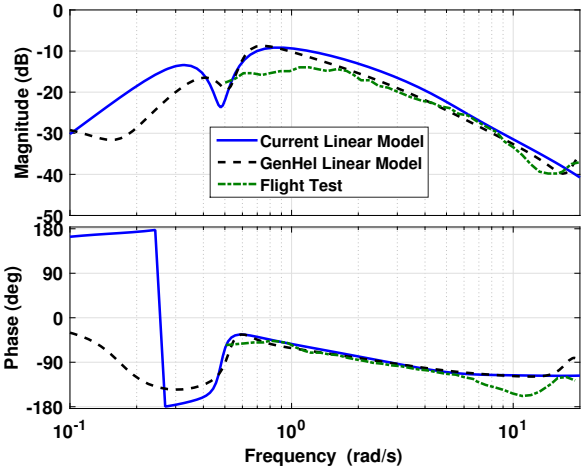

(b) Hover - q/δ_{long}

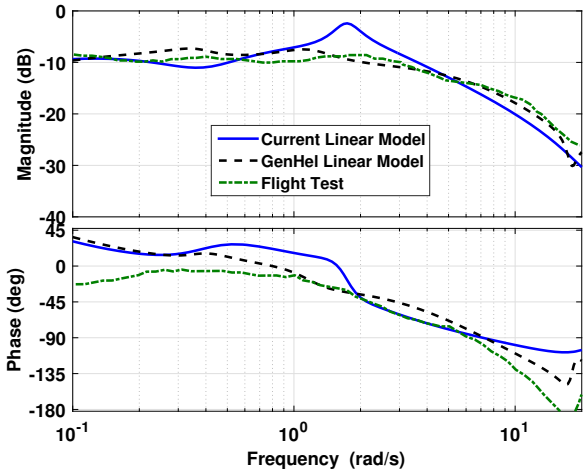

(c) 80 knots - p/δ_{lat}

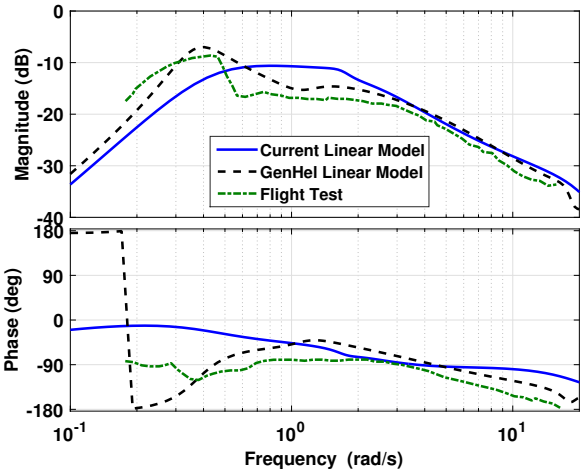

(d) 80 knots - q/δ_{long}

Fig. 2: Baseline UH-60A Frequency Response Validation

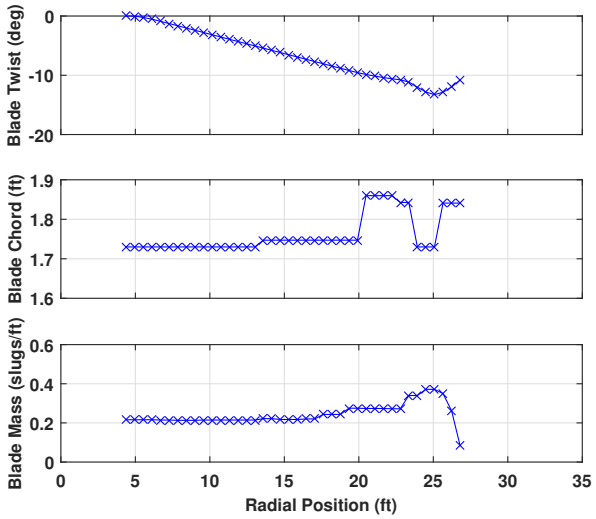

(a) Baseline UH-60A blade

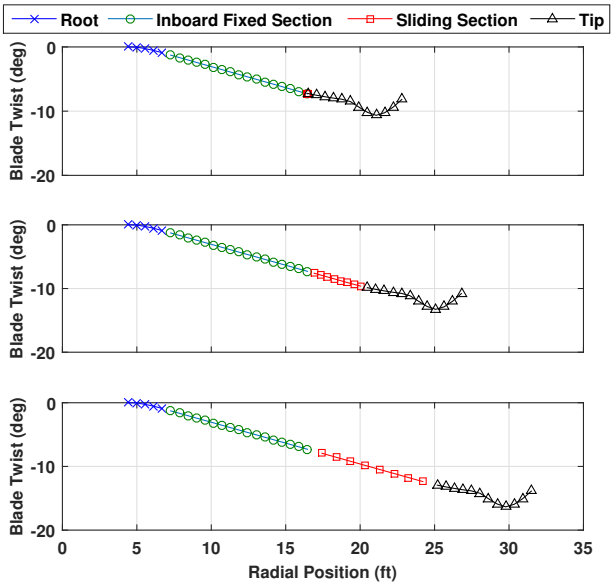

(b) Variable span blade - Twist Distribution

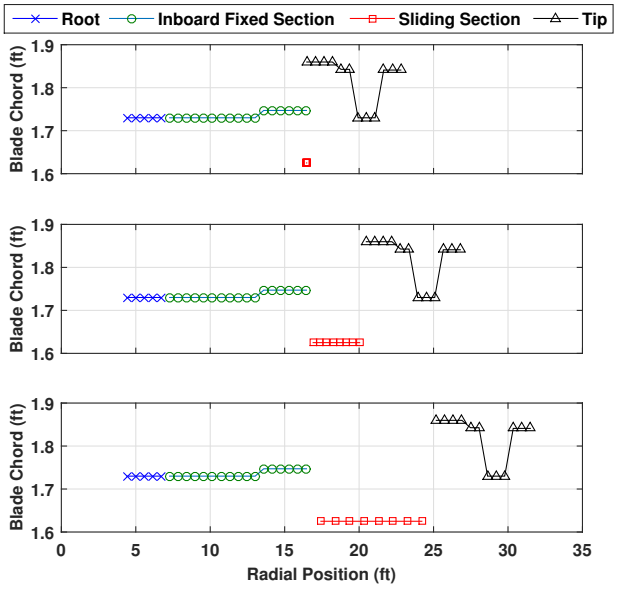

(c) Variable span blade - Chord Distribution

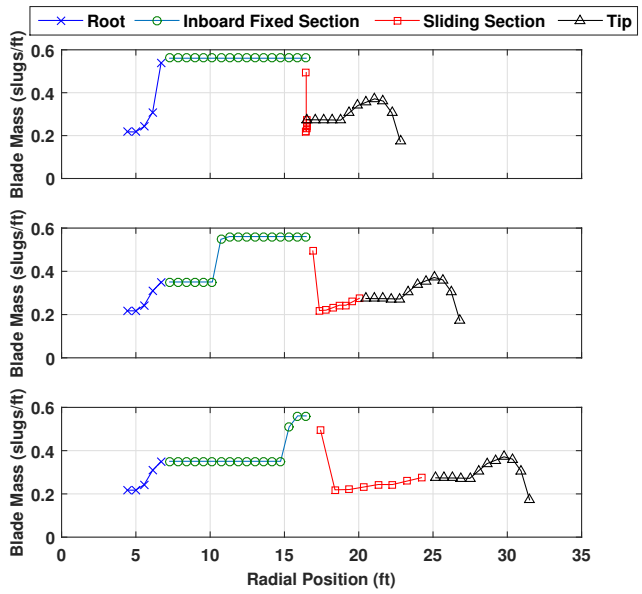

(d) Variable span blade - Mass Distribution

Fig. 3: Blade Properties - Baseline vs Variable Span

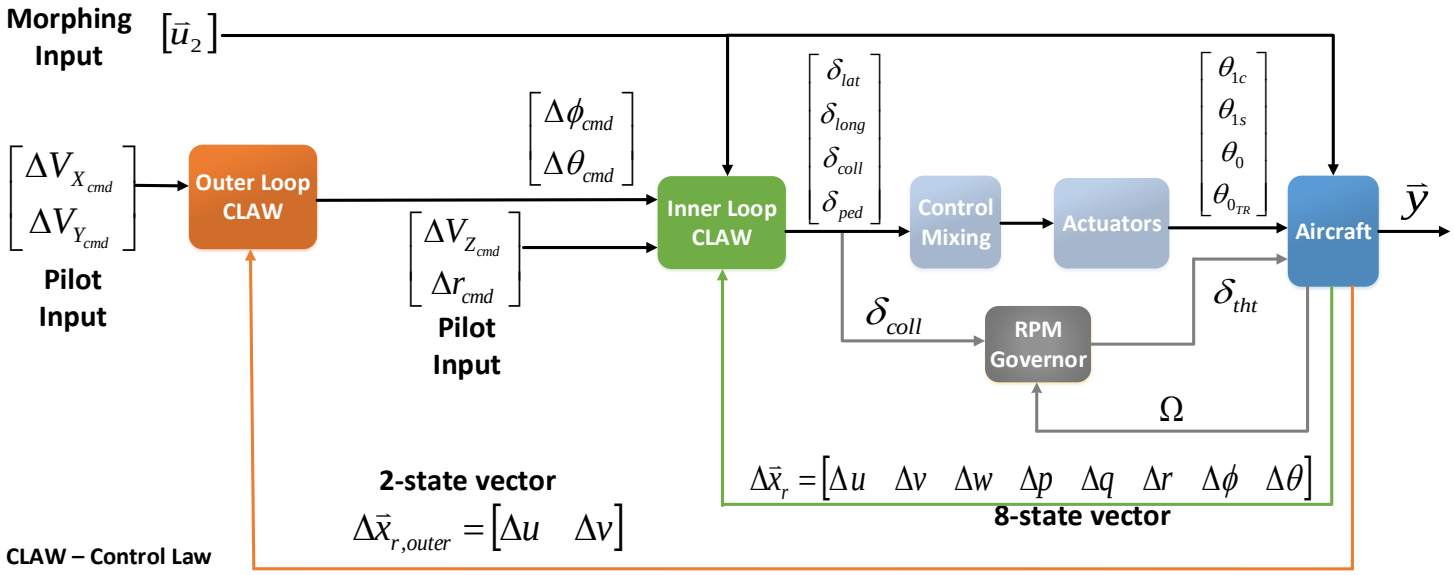

Fig. 4: Overview of the Control System

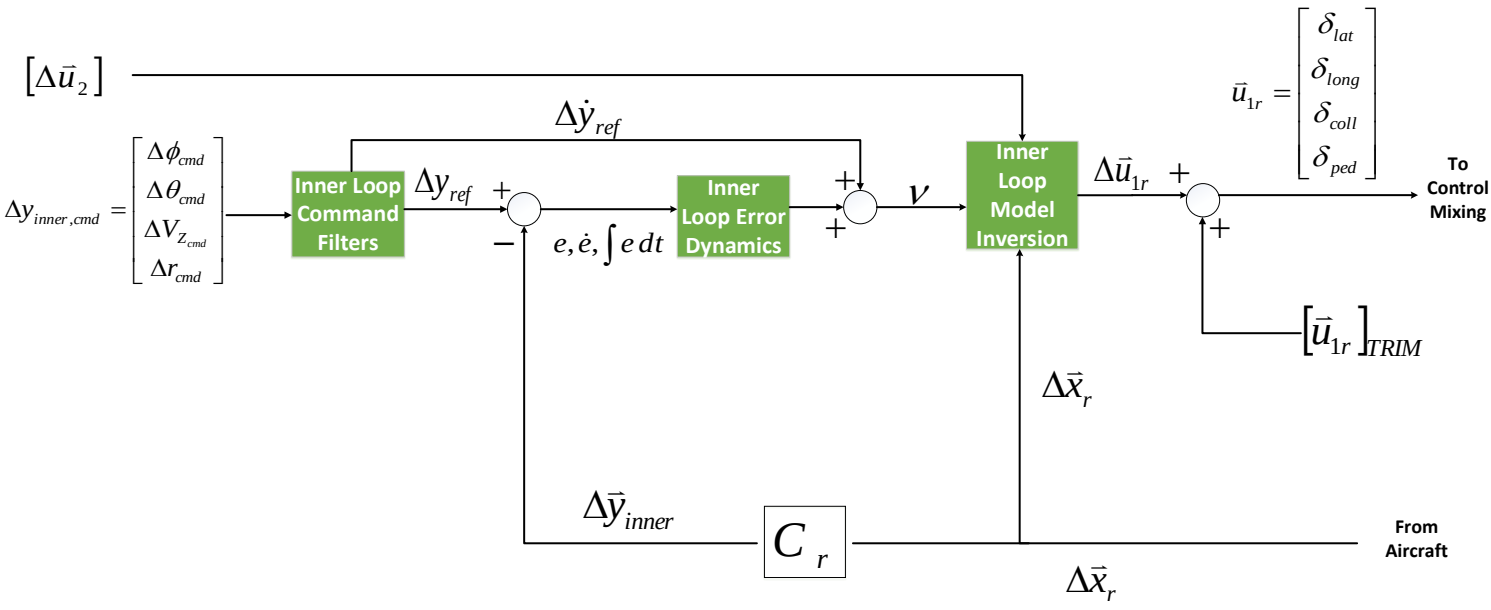

Fig. 5: Inner Loop CLAW

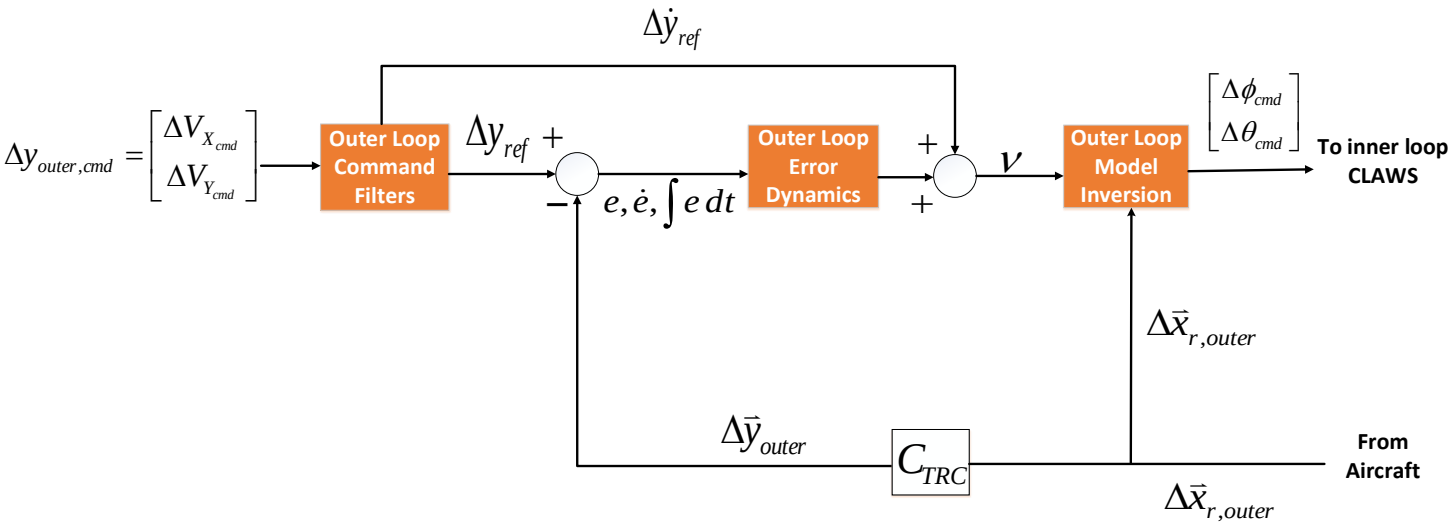

Fig. 6: Outer Loop CLAW

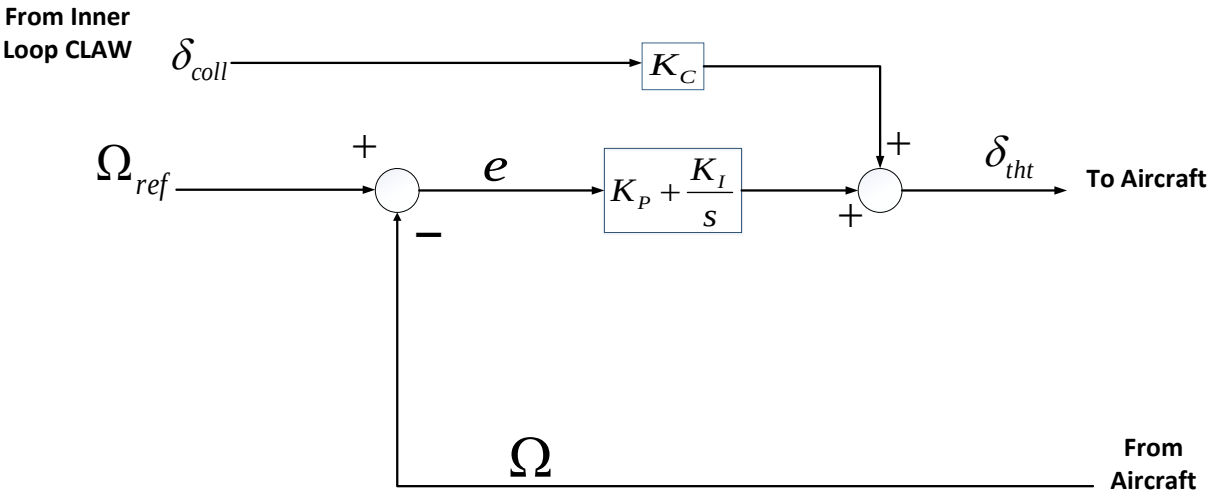

Fig. 7: RPM Governor

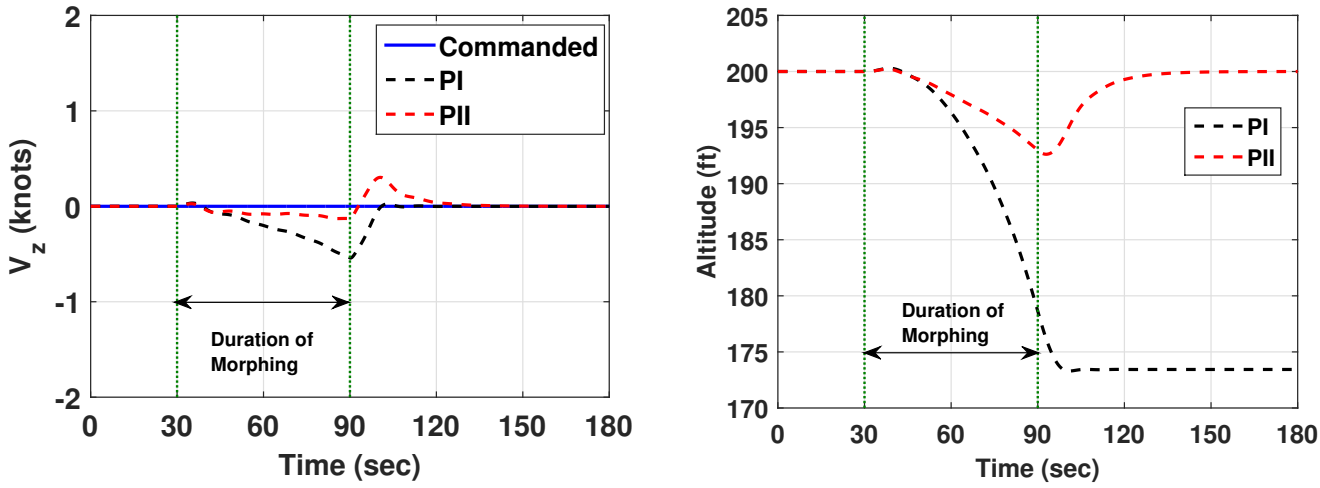

(a) Vertical Speed

(b) Inertial Position

Fig. 8: Heave Velocity and Inertial Position - Hover: PI vs PII

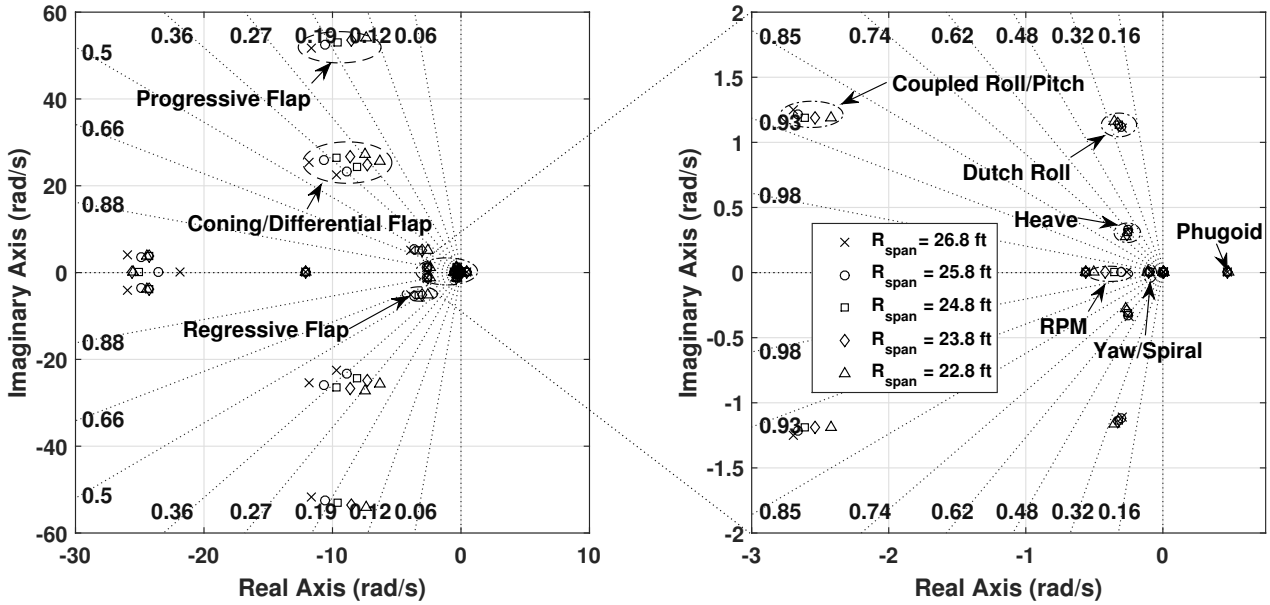

(a) Open-loop eigenvalues - 40 knots retraction

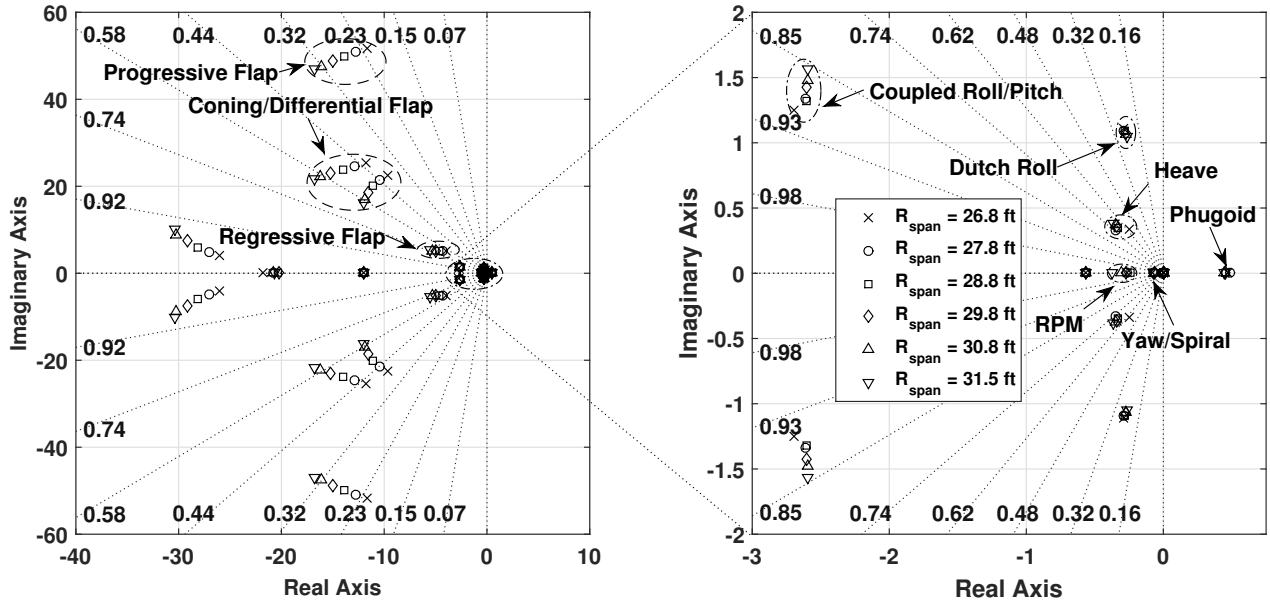

(b) Open-loop eigenvalues - 40 knots extension

Fig. 9: Bare Airframe (open-loop) eigenvalues at 40 knots

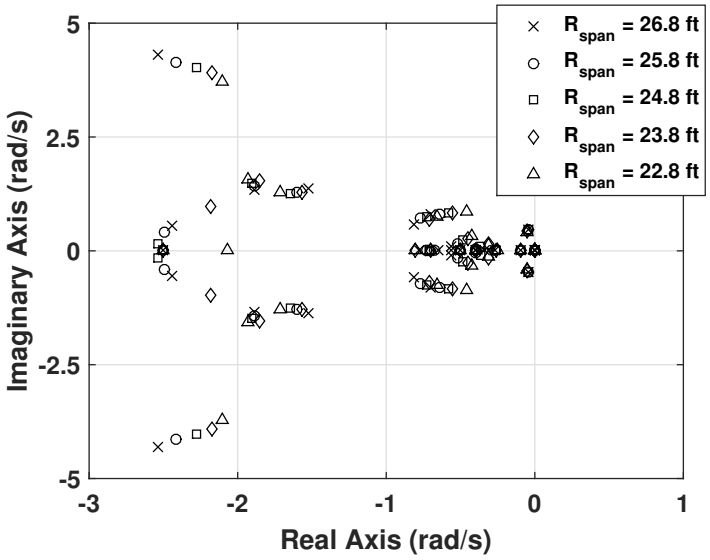

(a) Closed-loop eigenvalues - 40 knots retraction

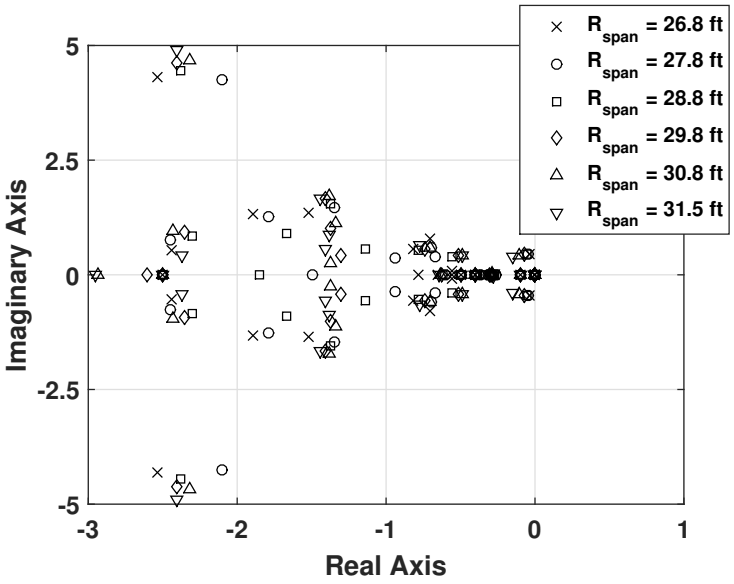

(b) Closed-loop eigenvalues - 40 knots extension

Fig. 10: Closed-loop eigenvalues at 40 knots

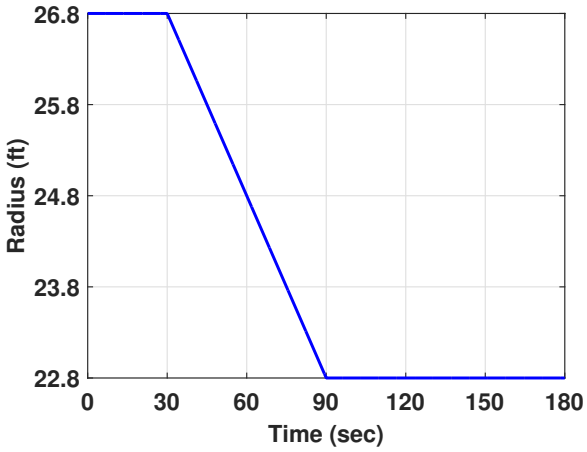

(a) Blade Radius

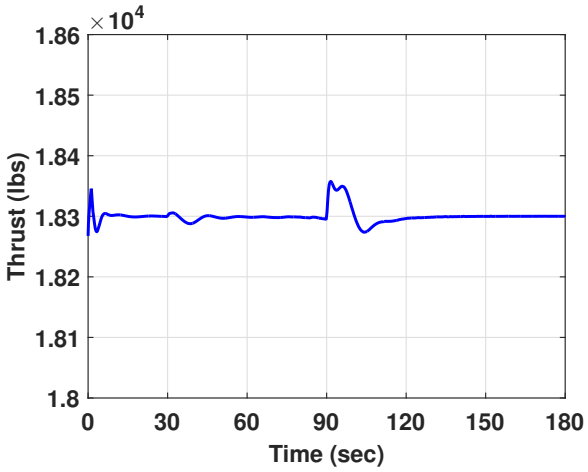

(b) Aircraft Thrust

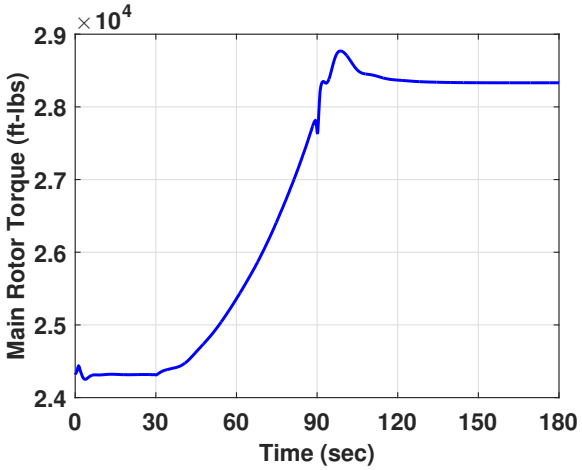

(c) Main Rotor Torque

Fig. 11: 40 knots retraction - Radius, Thrust, and Torque

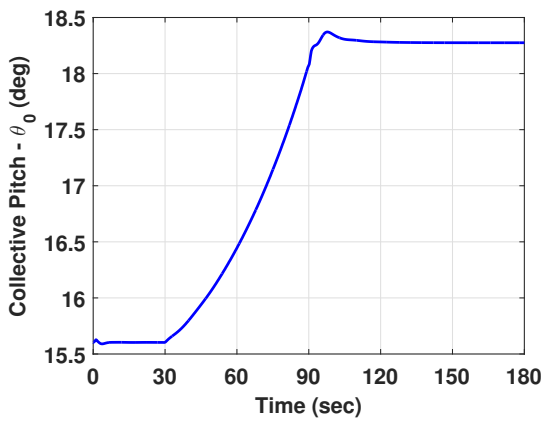

(a) Collective Pitch

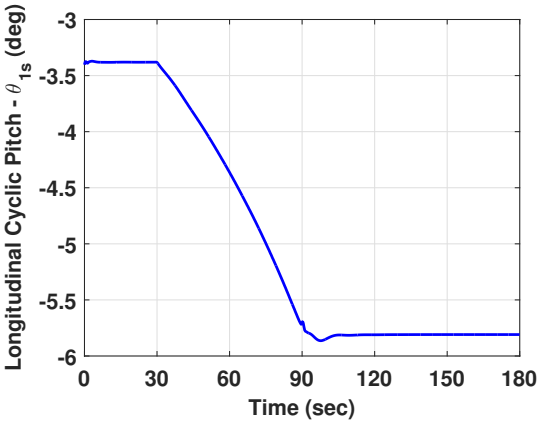

(b) Longitudinal Cyclic Pitch

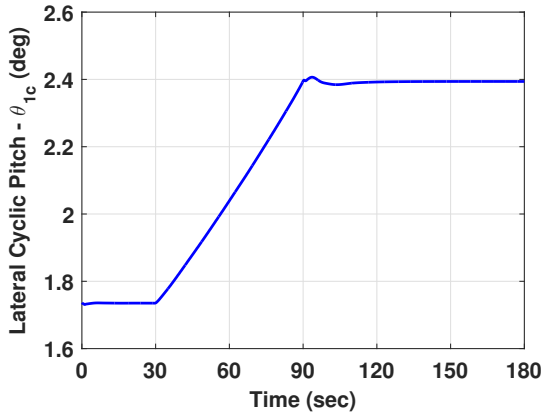

(c) Lateral Cyclic Pitch

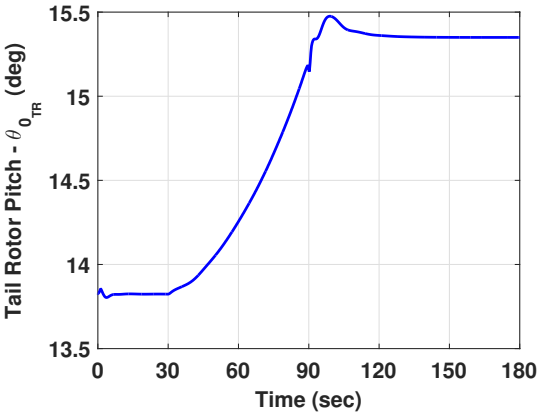

(d) Tail Rotor Collective Pitch

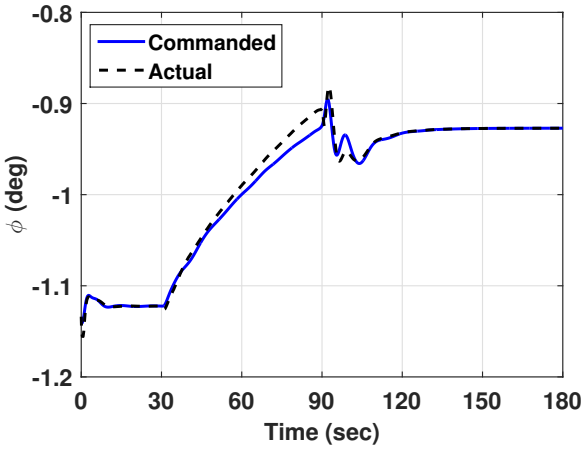

(e) Roll Attitude

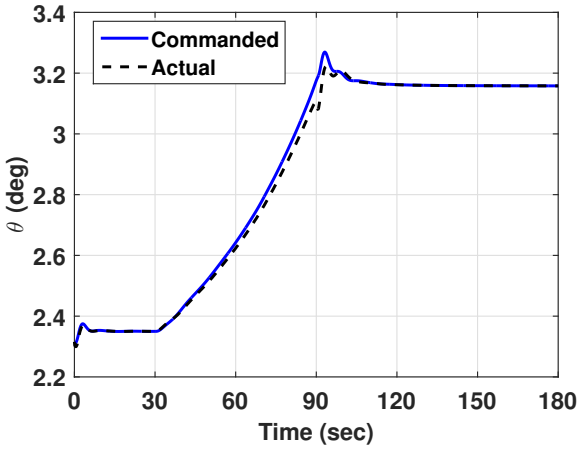

(f) Pitch Attitude

Fig. 12: 40 knots retraction - Controls and Attitudes (θ is positive nose up, ϕ is positive roll right)

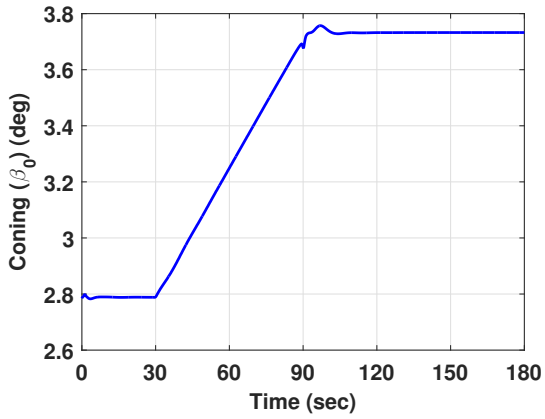

(a) Coning

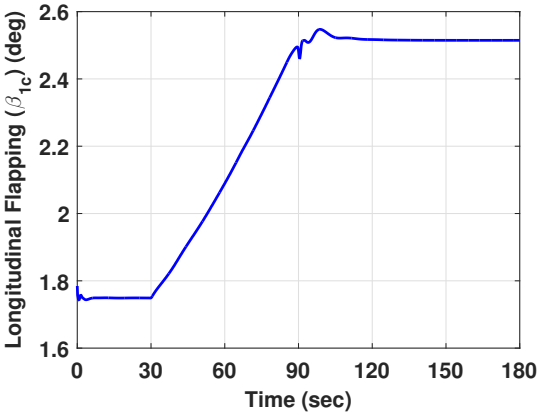

(b) Longitudinal Flapping

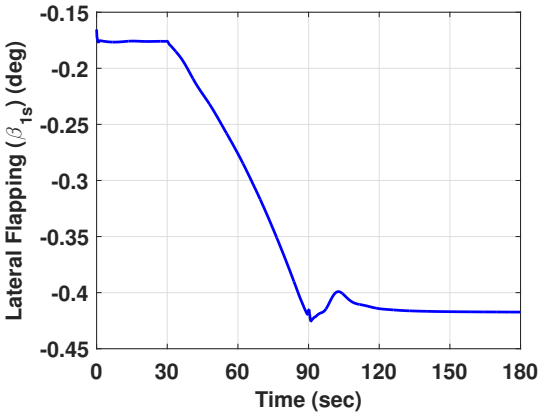

(c) Lateral Flapping

Fig. 13: 40 knots retraction - Flapping

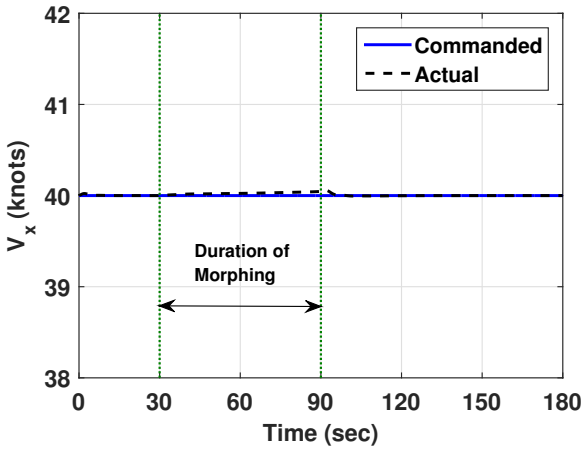

(a) Longitudinal Ground Speed

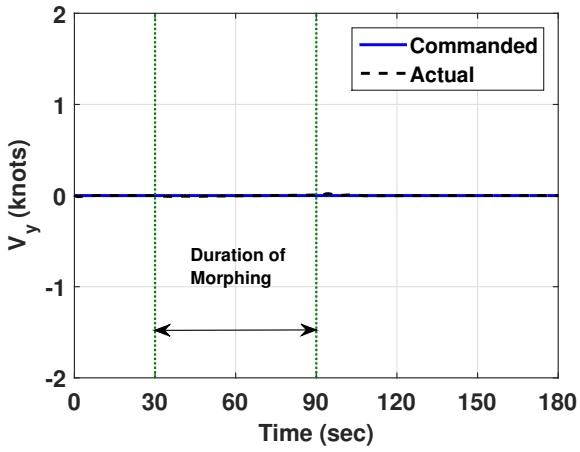

(b) Lateral Ground Speed

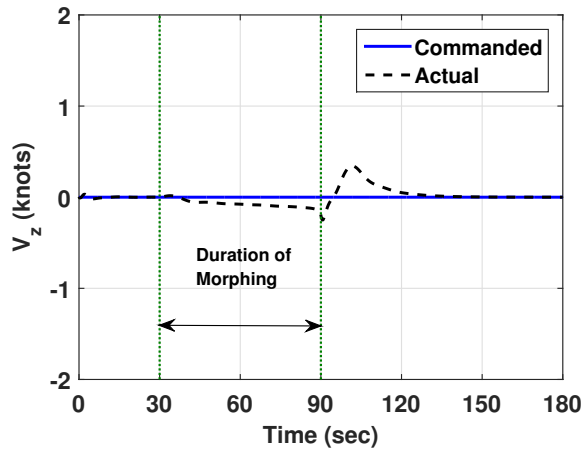

(c) Vertical Speed

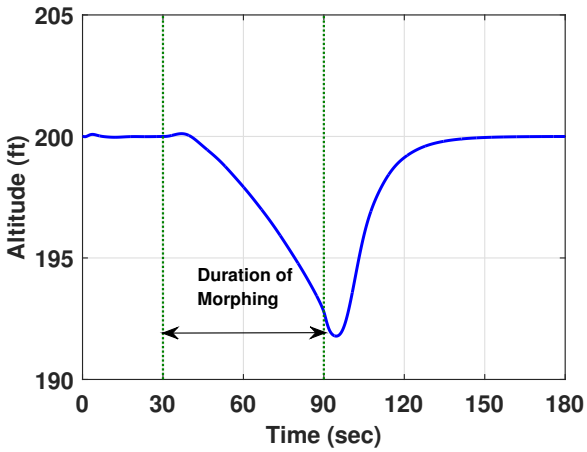

(d) Altitude

Fig. 14: 40 knots retraction - Inertial Velocities and Altitude

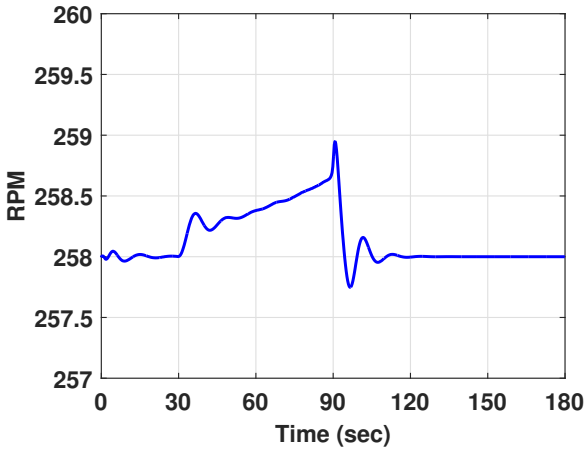

Fig. 15: 40 knots retraction - RPM

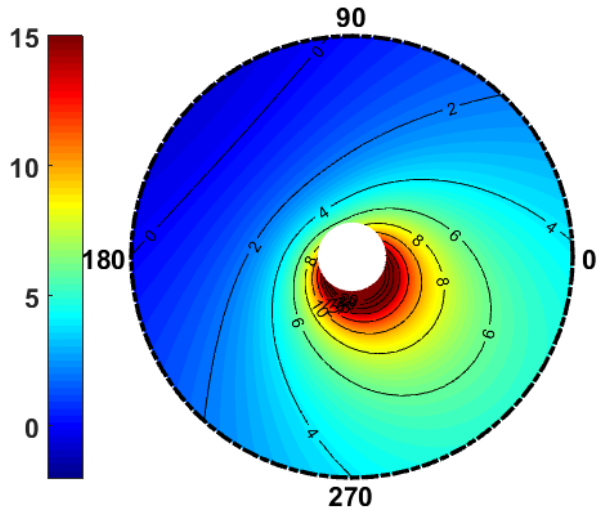

(a) Elemental Inflow Angle (deg), $R_{span} = 26.8$ ft

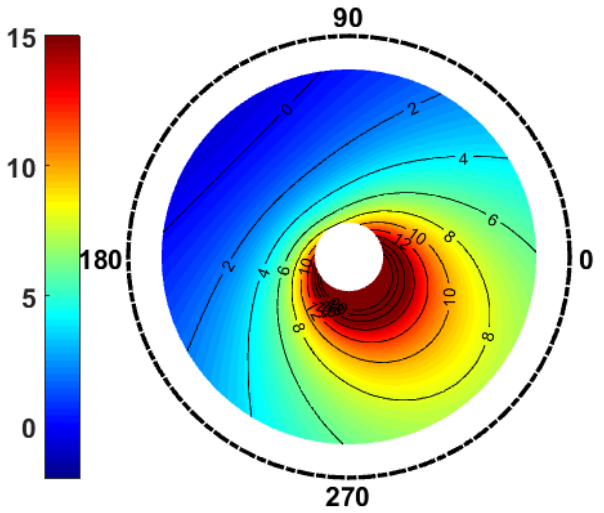

(b) Elemental Inflow Angle (deg), $R_{span} = 22.8$ ft

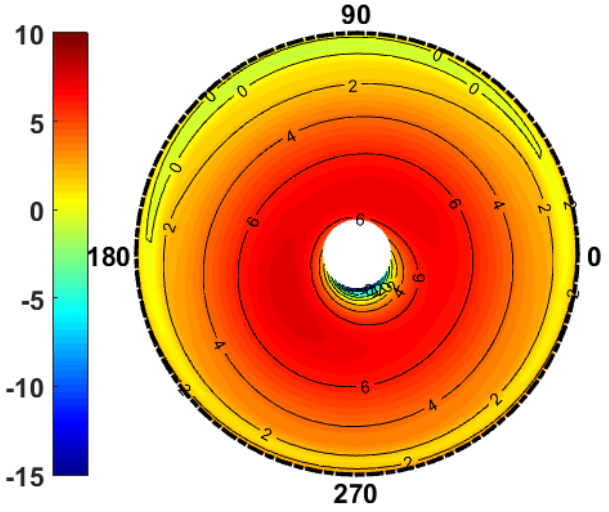

(c) Elemental Angle of attack (deg), $R_{span} = 26.8$ ft

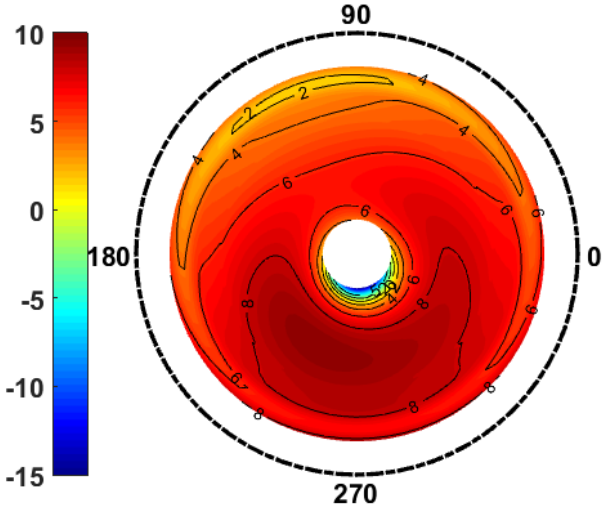

(d) Elemental Angle of attack (deg), $R_{span} = 22.8$ ft

Fig. 16: 40 knots retraction - Induced inflow angle (ϕ_i) and Angle of attack (α) distribution

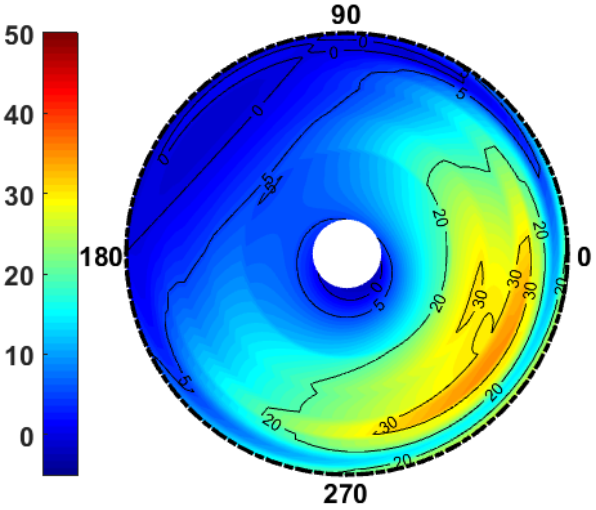

(a) Elemental Induced Drag (lbs/ft), $R_{span} = 26.8$ ft

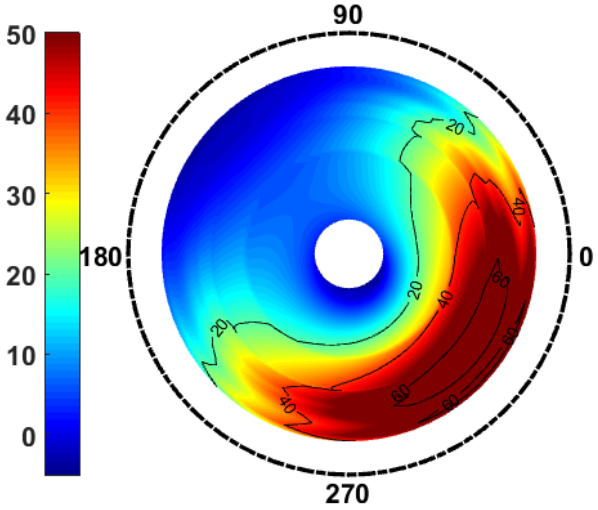

(b) Elemental Induced Drag (lbs/ft), $R_{span} = 22.8$ ft

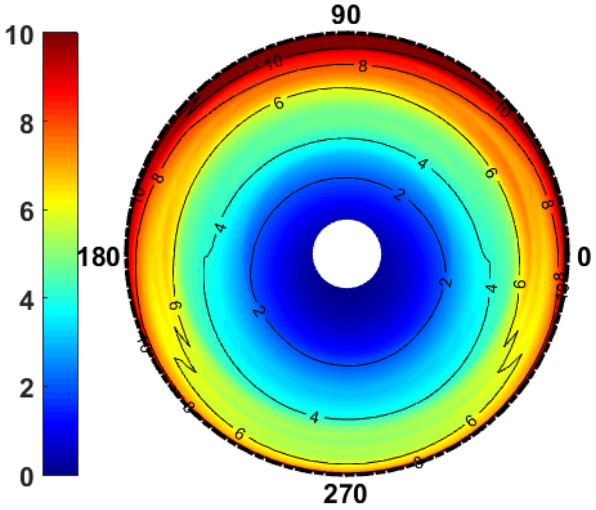

(c) Elemental Profile Drag (lbs/ft), $R_{span} = 26.8$ ft

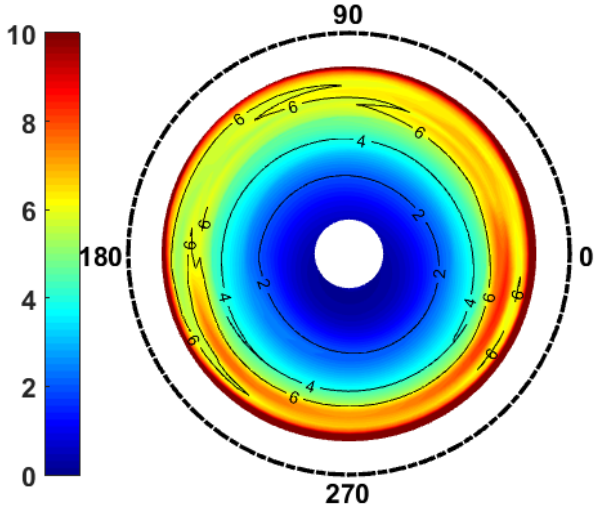

(d) Elemental Profile Drag (lbs/ft), $R_{span} = 22.8$ ft

Fig. 17: 40 knots retraction - Induced and Profile Drag Distribution

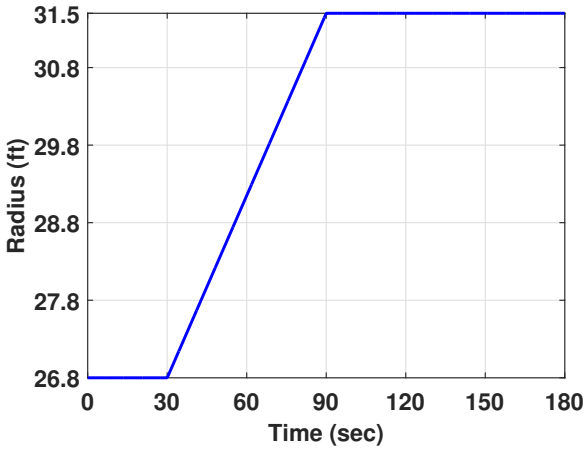

(a) Blade Radius

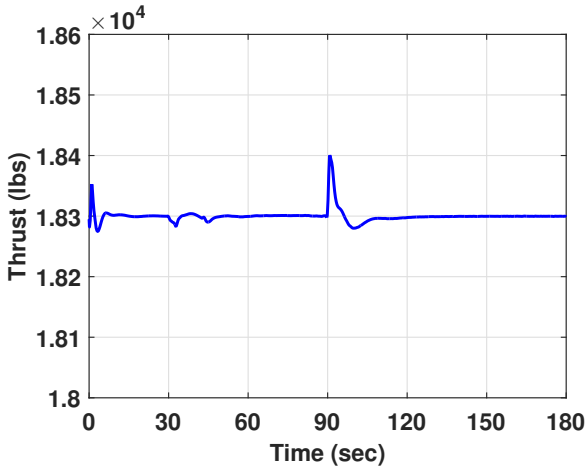

(b) Aircraft Thrust

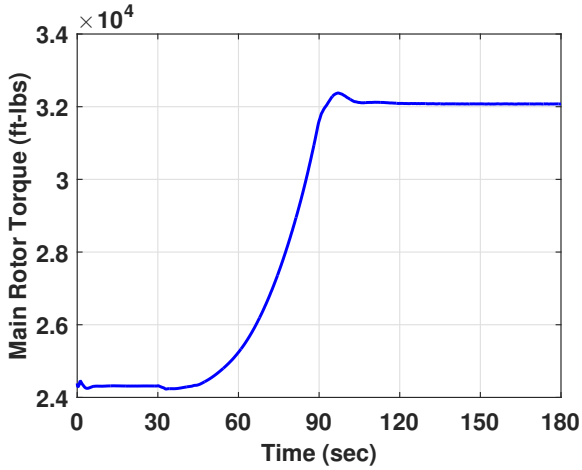

(c) Main Rotor Torque

Fig. 18: 40 knots extension - Radius, Thrust, and Torque

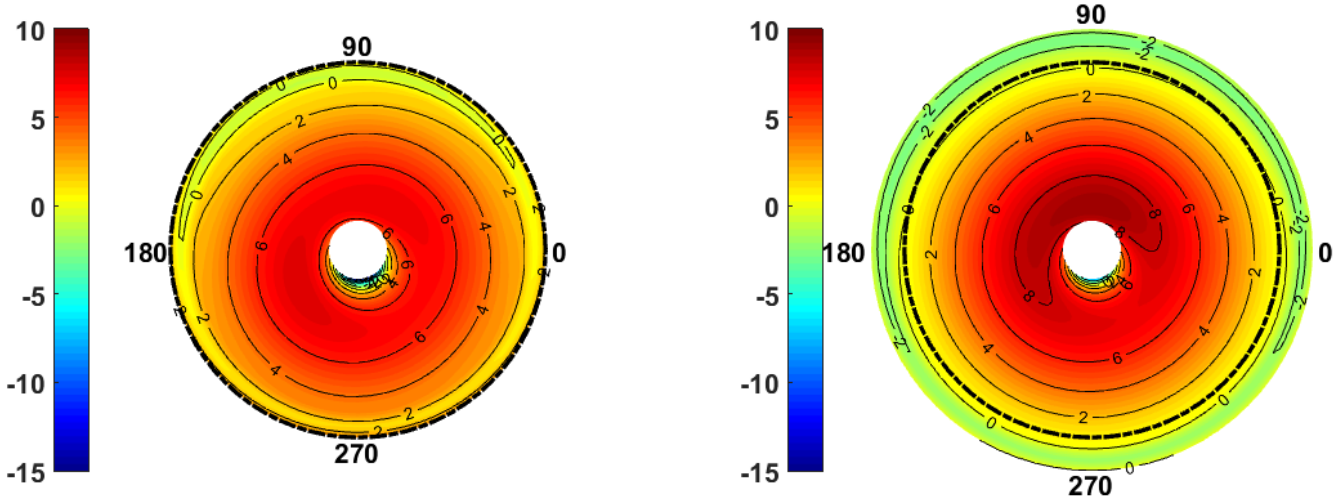

(a) Elemental Angle of attack (deg), $R_{span} = 26.8$ ft

(b) Elemental Angle of attack (deg), $R_{span} = 31.5$ ft

Fig. 19: 40 knots extension - Angle of attack (α) distribution

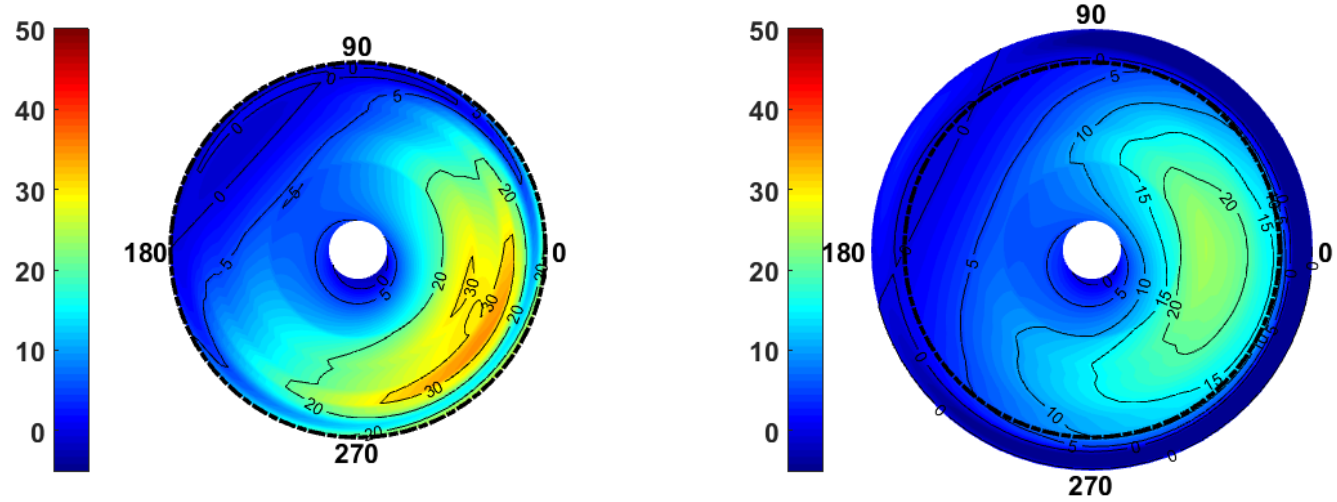

(a) Elemental Induced Drag (lbs/ft), $R_{span} = 26.8$ ft

(b) Elemental Induced Drag (lbs/ft), $R_{span} = 31.5$ ft

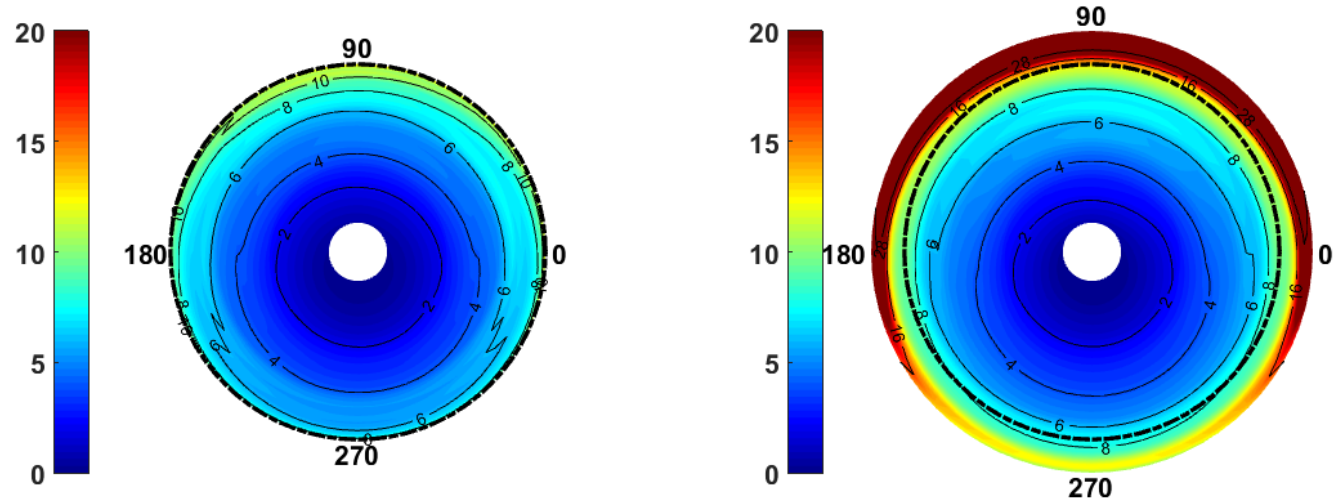

(c) Elemental Profile Drag (lbs/ft), $R_{span} = 26.8$ ft

(d) Elemental Profile Drag (lbs/ft), $R_{span} = 31.5$ ft

Fig. 20: 40 knots extension - Induced and Profile Drag Distribution

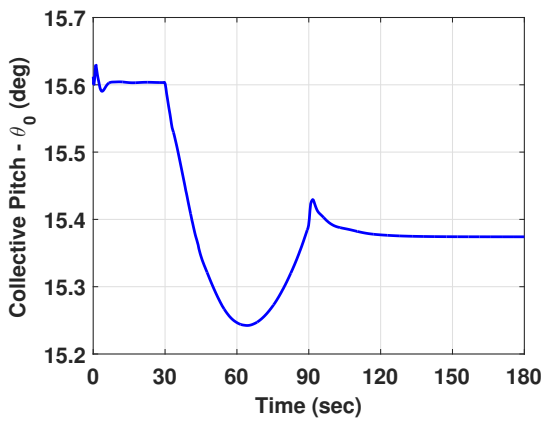

(a) Collective Pitch

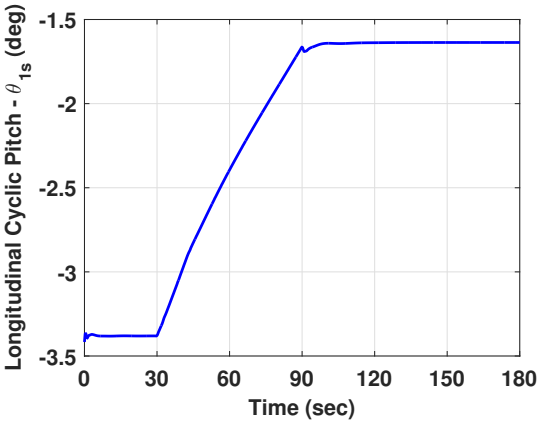

(b) Longitudinal Cyclic Pitch

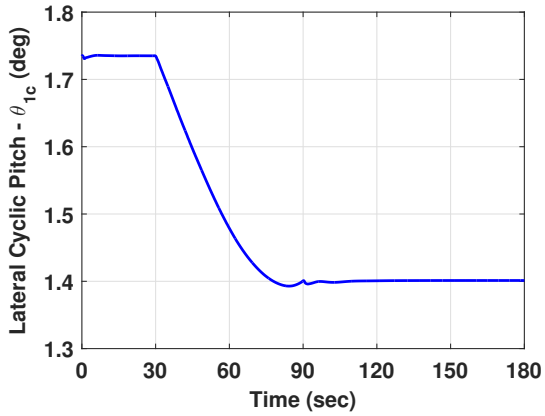

(c) Lateral Cyclic Pitch

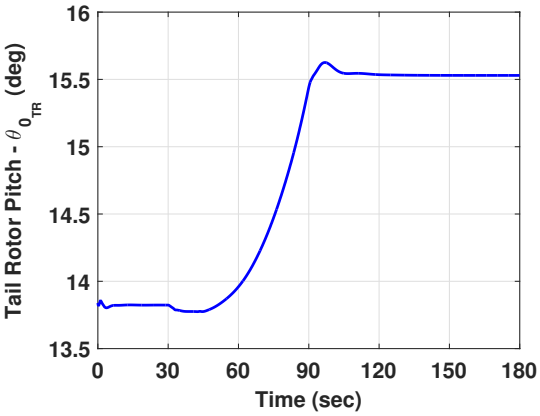

(d) Tail Rotor Pitch

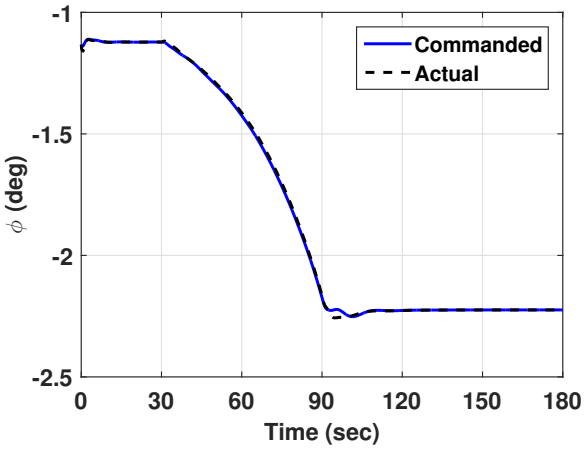

(e) Roll Attitude

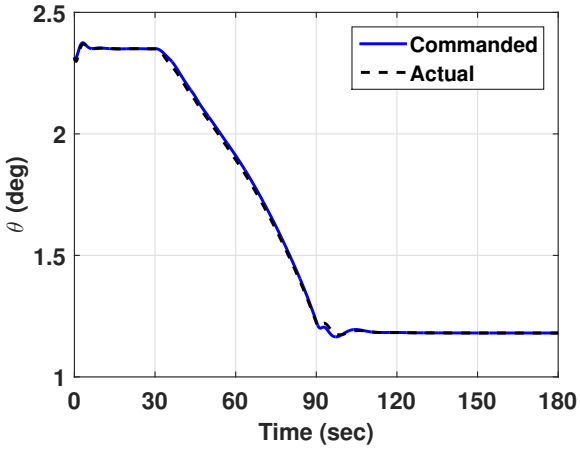

(f) Pitch Attitude

Fig. 21: 40 knots extension - Controls and Attitudes (θ is positive nose up, ϕ is positive roll right)

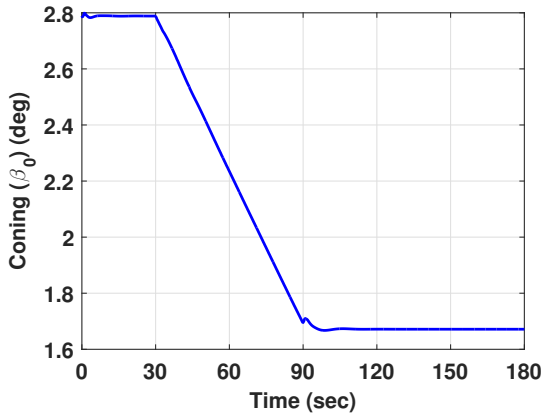

(a) Coning

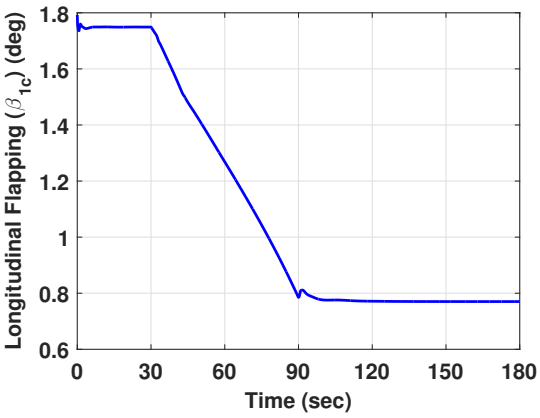

(b) Longitudinal Flapping

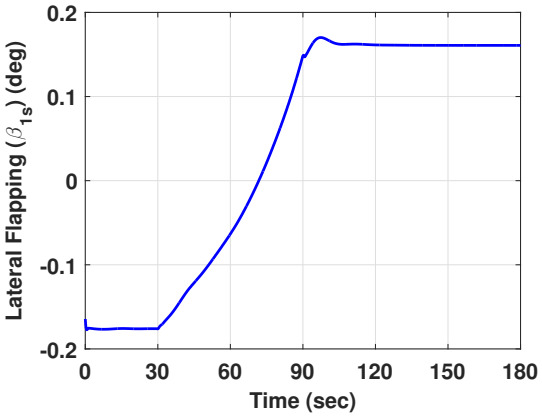

(c) Lateral Flapping

Fig. 22: 40 knots extension - Flapping

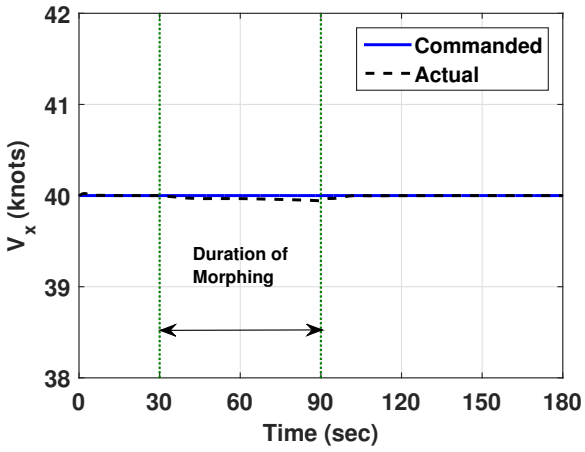

(a) Longitudinal Ground Speed

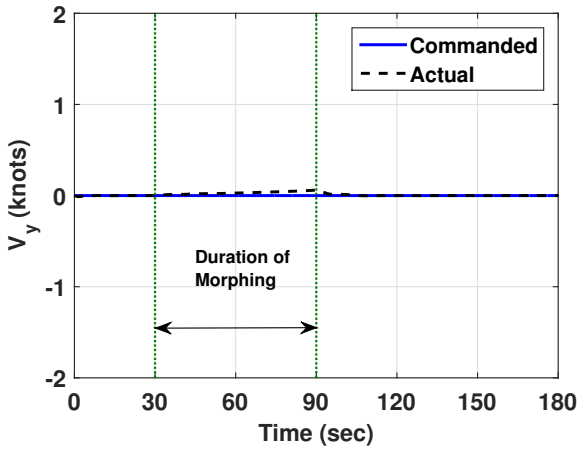

(b) Lateral Ground Speed

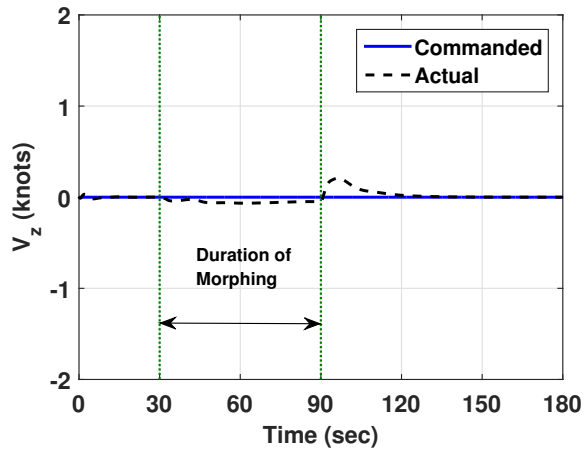

(c) Vertical Speed

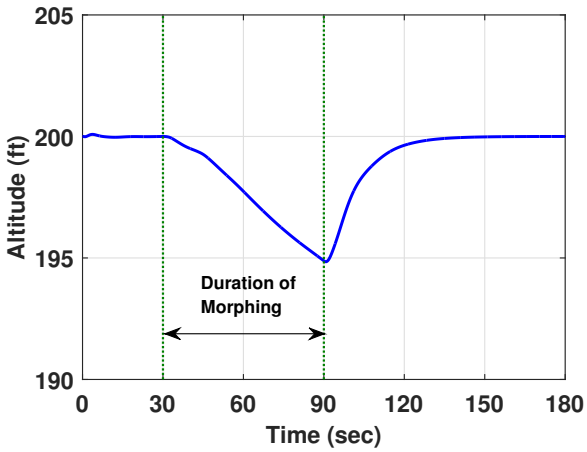

(d) Altitude

Fig. 23: 40 knots extension - Inertial Velocities and Altitude

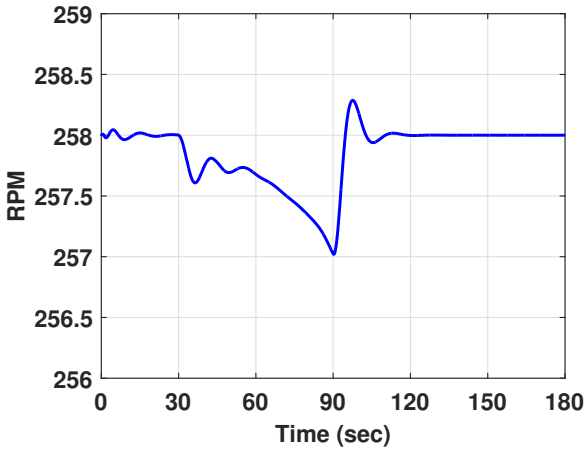

Fig. 24: 40 knots extension - RPM

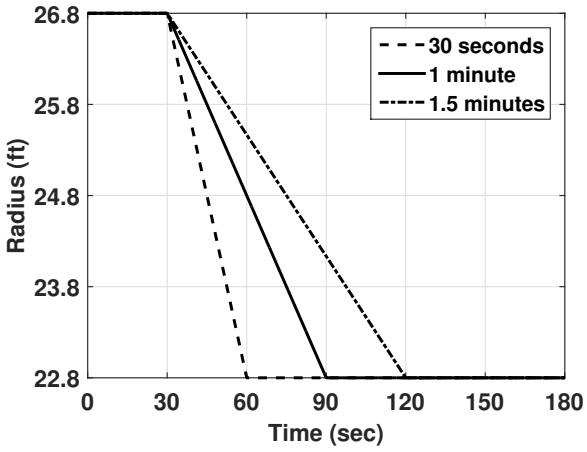

(a) Blade Radius

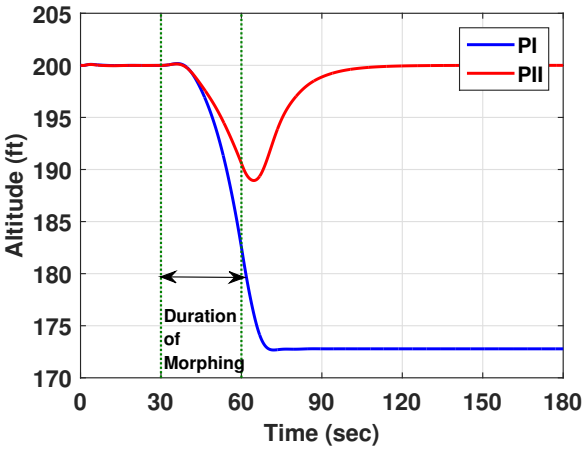

(b) Altitude

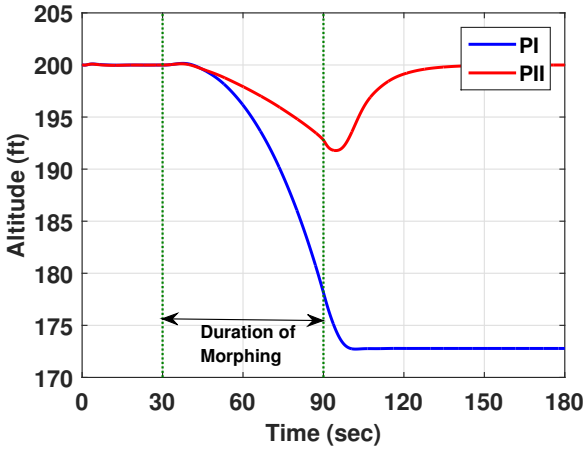

(c) Altitude

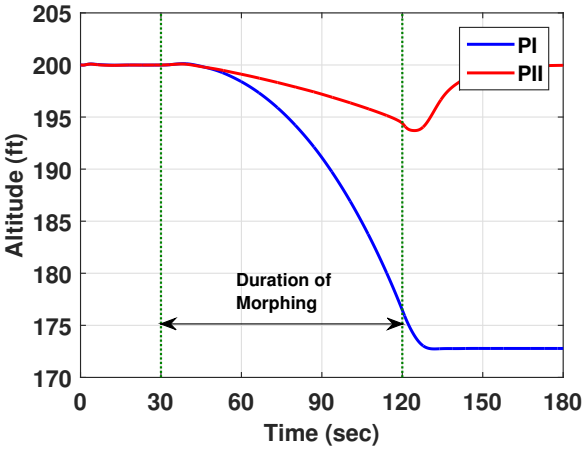

(d) Altitude

Fig. 25: Rate of Retraction - 40 knots

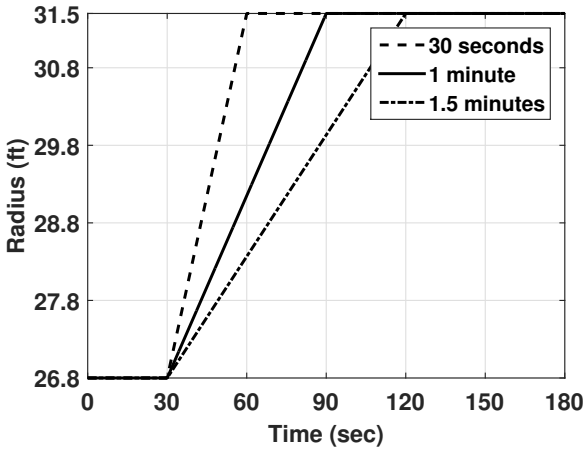

(a) Blade Radius

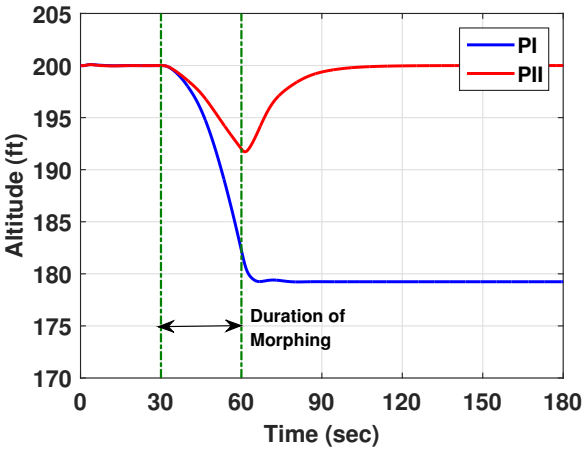

(b) Altitude

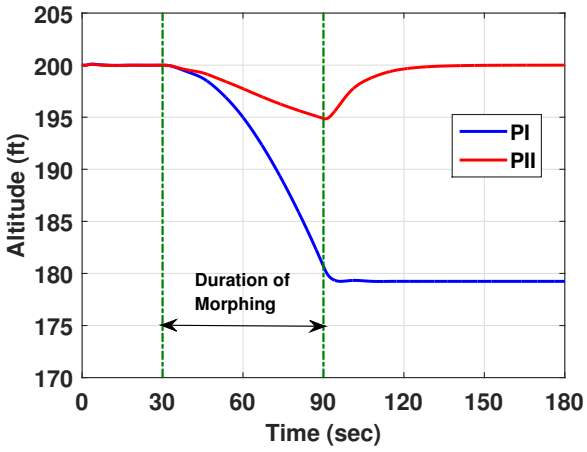

(c) Altitude

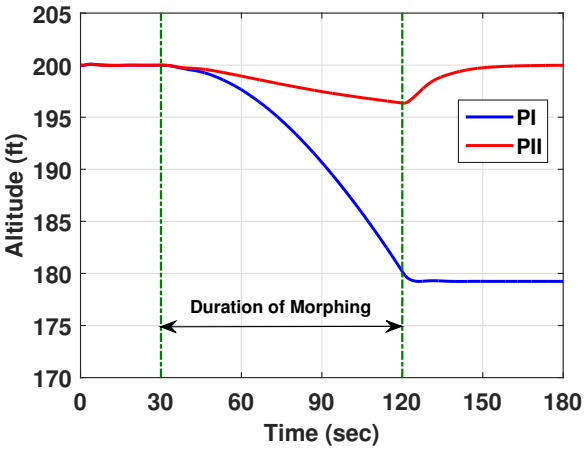

(d) Altitude

Fig. 26: Rate of Extension - 40 knots